REVIEW

The *SINQ Target Irradiation Program* (STIP) has been developed at *Paul Scherrer Institute* (PSI) during the last twenty years. It is aimed to analyze the radiation damage induced by spallation reactions in different structural materials. It is also providing relevant data for developing future spallation sources as well as advanced spallation targets.

STIP VI was conducted in SINQ Target 9 during 2011/2012 receiving a total proton charge of 13.16 Ah. The *Monte Carlo N-Particle eXtended code* (MCNPX) is used for implementing the model and performing the simulation to obtain the proton and neutron fluences as well as the energy deposition in the different points of interest. Afterwards, this information is used for calculating the displacement per atom (dpa) plus the Helium and Hydrogen production in atomic parts per million (appm). The results will contribute to understand the irradiation effect in different structural materials. It will also be useful for comparing it with the real radiation damage measurements of the irradiated materials after its cool down period.

The target mainly consists of the AlMg3 inverted semi-sphere Beam Entrance Window (BEW) and the cylindrical Rod Container Box (RCB) which keeps inside 306 rods fitting 36 rows. There is also the Safety Hull Tube (SHT), made of AlMg3, which consists of a double cylinder walls surrounding the RCB and linked to the inverted BEW at the bottom. The source definition is implemented in the MCNPX input file from the gamma mapping performed at the irradiated Target 9. The material specification of the specimen rods is implemented by taking its average composition, assuming a uniform distribution.

The maximum proton flux obtained at the inverted BEW is 1.75×10^{14} p/(cm^2·s·mA). The maximum proton fluence in the target is obtained in Row 0 becoming 8.33×10^{25} p/m^2. The maximum neutron fluence is obtained in Row 8 with a value of 1.99×10^{26} n/m^2, which in flux units stands for 4.19×10^{14} n/(cm^2·s·mA). Regarding the SHT, the maximum proton flux escaping from the target is obtained above Row 36 with a value of 5.99×10^{11} p/(cm^2·s·mA) and the maximum neutron flux is escaping around the middle part of the target with a value of 1.39×10^{14} n/(cm^2·s·mA). The maximum energy deposition in Zircaloy-2 cladding tubes is obtained in the center rod placed in Row 2 with a value of 400.32 W/(cm^3·mA).

The irradiation parameters have been calculated by multiplying the proton and neutron fluence with its corresponding material cross section data. The results obtained at the center of the inverted BEW are 8.85 dpa, 2447 appm He and 4854 appm H. For the SHT, the maximum values of the irradiation parameters are obtained around the middle part of the target with the following values: 3.14 dpa, 17.63 appm He and 71.64 appm H.

Finally, the maximum displacement per atom in the specimen rods is obtained for Zircaloy-2 in Rod 1, placed in Row 2, with a value of 72.07 dpa and the maximum Helium & Hydrogen concentration are obtained for Tantalum in Rod A, placed in Row 1, with the following values: 3629 appm He and 17418 appm H.

TABLE OF CONTENTS

GLOSSARY

appm	Atomic parts per million
BB	Bend Bar
BEW	Beam Entrance Window
CEA	Commissariat à l'Energie Atomique et aux Énergies alternatives
dpa	Displacement per atom
E_d	Threshold Displacement Energy
FZJ	Forschungszentrum Jülich
JAERI	Japanese Atomic Energy Research Institute
LANL	Los Alamos National Laboratory
LBE	Lead Bismuth Eutectic
LMT	Liquid Metal Target
LT	Large Tensile
MCNPX	Monte Carlo N-Particle eXtended
ORNL	Oak Ridge National Laboratory
PKA	Primary Knock-on Atom
PSI	Paul Scherrer Institute
RCB	Rod Container Box
SμS	Swiss Muon Source
SINQ	Swiss Spallation Neutron Source
SHT	Safety Hull Tube
SLS	Swiss Light Source
ST	Small Tensile
STIP	SINQ Target Irradiation Program
TEM	Transmission Electron Microscope

1. INTRODUCTION

The *Paul Scherrer Institute* (PSI) is one of the most powerful research centers worldwide. It is located in the Canton of Aargau, Switzerland, in the municipal areas of Villigen and Würenlingen, on both sides of the river Aare. The main fields of research are Matter and Materials, Energy and Environment and Health. The research in the field of Matter and Materials is mainly focused on the internal structure of a wide range of different materials. The results are contributing to a better understanding of the processes occurring in nature as well as providing starting points in the development of new materials for technical applications. In the Energy and Environment area, the main research activities are related with the development of new technologies to facilitate the creation of a sustainable and secure energy supply taking care of the environment. Finally, researchers in the Health area are looking for the causes of illnesses to explore potential treatment methods.

The PSI is operating large research facilities which provide excellent conditions for Research and Development activities. These large facilities are: the *Swiss Light Source* (SLS), the *Swiss Spallation Neutron Source* (SINQ) and the *Swiss Muon Source* (SμS). The SLS is a third-generation synchrotron light source which provides photon beams of high brightness for research in materials science, biology and chemistry. The SμS is used for research in experiments related with understanding magnetic processes in solids and testing the Standard Model of elementary particle physics predictions. Lastly, the SINQ is a 1MW class research spallation neutron source providing a continuous flux of about 10^{14} n/(cm^2·s). It has been designed to provide two beam lines of thermal and cold neutrons for research purposes. The main scientific disciplines taking advantage of the SINQ facility are condensed matter physics and materials science. However, it is also used for isotope production with neutrons, neutron activation analysis, fission product physics and nuclear physics with polarized neutrons. A detailed description of how the proton beam is generated at the SINQ facility is presented by W. Wagner in "*TARGET OPERATION AT THE HIGH-POWER NEUTRON SPALLATION SOURCE SINQ – SAFETY AND RELIABILITY ISSUES*" [1].

One of the most important research programs carried out at the PSI SINQ Facility is the *SINQ Target Irradiation Program* (STIP). It was initiated in 1996 in collaboration with *Commissariat à l'Energie Atomique et aux Énergies alternatives* (CEA), *Forschungszentrum Jülich* (FZJ), *Japanese Atomic Energy Research Institute* (JAERI), *Los Alamos National Laboratory* (LANL) and *Oak Ridge National Laboratory* (ORNL). The main program's aim is studying the radiation damage induced by spallation in different structural materials. The research takes into account the Helium and Hydrogen production as well as the liquid metal effects on structural materials for understanding the radiation phenomena in an intensive irradiation environment. However, it is also being really important for under-going projects on developing future spallation sources and providing materials data for advanced spallation targets.

The spallation reaction is a process in which a light projectile like protons or neutrons with a high kinetic energy, from hundreds of MeV to several GeV, interacts with a heavy nucleus, as lead or tungsten. It produces an intra-nuclear cascade of high energy (greater than 20 MeV) protons, neutrons and pions within the nucleus. During the intra-nuclear cascade, some of these energetic hadrons escape as secondary particles. The other ones deposit their kinetic energy in the nucleus leaving it in an excited state. Then, the heavy nucleus relaxes by emitting a large number of low-energy hadrons (less than 20 MeV) which are mostly neutrons. The secondary high-energy particles produced during the intra-nuclear cascade can also collide with other target nuclei resulting in secondary spallation reactions which generate more secondary particles and low-energy neutrons. The low-energy neutrons produced during the nuclear de-excitation are really important in research because they can be moderated to even lower energies becoming in thermal and cold neutrons. A spallation process of 1 GeV proton is illustrated next:

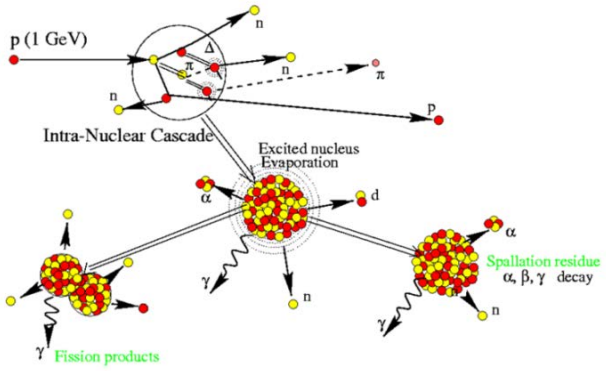

Figure 1.1 Spallation process for a 1 GeV proton [2]

The first SINQ Target Irradiation Program (STIP I) was carried out from July 1998 to December 1999 receiving a total proton charge of 6.8 Ah. In this experiment, more than 1500 samples of nearly 40 kinds of different materials were irradiated in a temperature range from 70°C to 410°C. The experiment was focused on comparing the different type of same base alloys, analyzing welded materials and studying advanced low-activation martensitic/ferritic steels developed for the fusion materials community. An extensive explanation of the experiment carried out containing the description of the materials and the specimen geometry is given by Y. Dai and G.S. Bauer (2001) [3].

The second SINQ Target Irradiation Program (STIP II) was performed in 2000 and 2001. The total proton charge received during this period was 10.03 Ah. In this experiment, more than 2000 specimen were irradiated up to 20 dpa and 1800 appm He in a temperature range of 80-450°C. A complete description of the experiment is given by Y. Dai [et al] (2005) [4].

Following the SINQ Target Irradiation Program, similar experiments have been also developed till nowadays: STIP III in 2002-03, STIP IV in 2004-05, STIP V in 2007-08 and STIP VI in 2011-12. All these experiments are concluded except STIP-VI which is close to finish the cooling down period. During all this time, a huge amount of different material samples has been analyzed increasing the range temperature up to 800°C. However, the major difference in these experiments is found on the SINQ Target.

The SINQ Target has been developed over the years in order to reach higher neutron flux in the target. The first targets, MARK I, were composed of solid zircaloy-2 rod bundles with a hexagonal cross section. In 2000, these rod bundles were replaced by lead filled stainless steel tube in a quadratic cross section (MARK II). In 2006, a Lead Bismuth Eutectic (LBE) Liquid Metal Target (LMT), named as MEGAPIE, was operated successfully providing neutron yields up to 80% higher. After that, MARK III targets were used in 2007-2008 changing the MARK II targets cladding from stainless steel to zircaloy-2 increasing again the neutron yield by about 6% in comparison with MARK II targets. Finally, STIP VI is using a MARK IV target which has been improved by surrounding the target with a lead filled reflector (blanket) with an inverted Beam Entrance Window (BEW) integrated in the double walled AlMg3 safety hull.

The proton and neutron fluences as well as heat deposition on STIP targets are computed using the *Monte Carlo N-Particle eXtended code* (MCNPX). The *Monte Carlo N-Particle Transport code* (MCNP) [5] is a software package used for analyzing the transport of neutrons, photons, electrons or a combination of them by the simulation of a huge number of particles. The MCNPX is a general purpose Monte Carlo radiation transport code designed to track many particle types over broad ranges of energies. The MCNPX is capable of simulating particle interactions of 34 different types of particles (nucleons and ions) and more than 2000 heavy ions at nearly all energies, including those simulated by MCNP.

The MCNP is applying Monte Carlo experiments which are very different from deterministic transport methods. Deterministic methods are solving the transport equation for the average particle behavior. By contrast, Monte Carlo obtains answers by simulating individual particles and recording some aspects of their average behavior. The average behavior of particles in the physical system is then inferred using the central limit theorem from the average behavior of the simulated particles.

Basically, the MCNPX works simulating a huge amount of particles from its birth in the source to its death in any of the terminal categories like absorption or escape. Probability distributions are randomly sampled using transport data in order to determine the outcome at each particle step during its life. A random history of a neutron incident on a slab of fissionable material that can undergo fission is illustrated in the next figure.

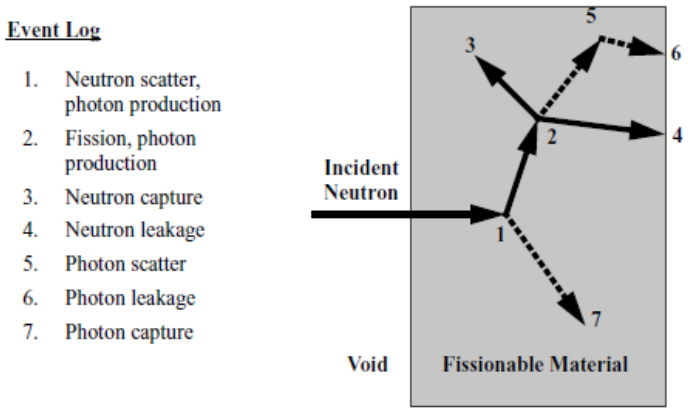

Figure 1.2 Random history of a neutron that can undergo fission [5]

The MCNPX input file contains the information necessary to describe the problem as well as the parameters which are characterizing the simulation for obtaining the results. An example of the general structure of a MNCPX input file is presented in *Figure 1.3*.

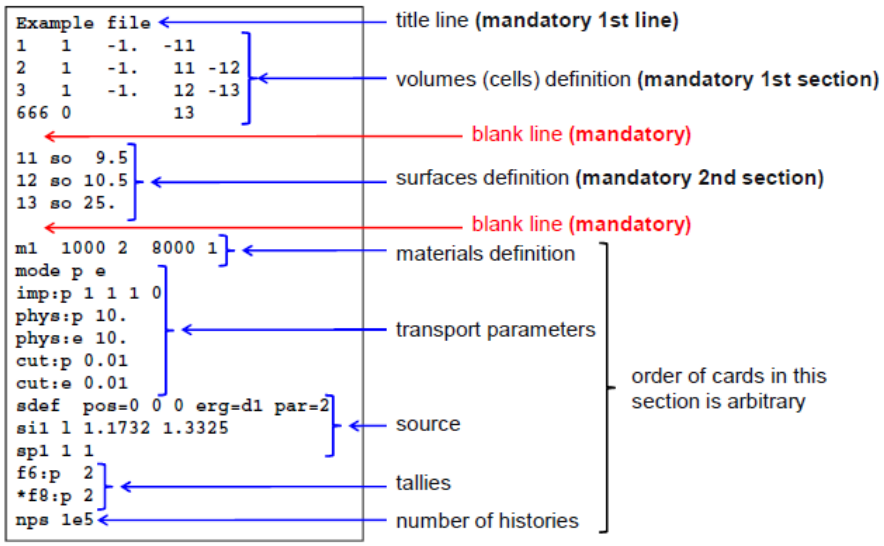

Figure 1.3 Structure of a MCNPX input file

The geometry problem is treated by MCNP in terms of volumes bounded by surfaces. The user is defining a cell by intersections, unions and complements of regions which are bounded by a surface, multiple surfaces or by infinity. The material specification is defined by a unique material number, the elemental (or isotopic) composition and the cross section compilation to be used. The material filling a cell is defined in the cell card definition by adding the unique material number and the density. It allows the user to define different densities in different cells for the same material. The source and type of radiation particles are specified by the SDEF command which contains many variables to define all the characteristics of all sources in the problem. The transport parameters are defined to characterize the simulation. The challenge in using MCNP is to minimize the computing expense needed to obtain a tally estimate with acceptable relative error as well as satisfying nine other statistical criteria which are also computed from the simulation. The usual method for limiting the computing time is to specify either the maximum number of source particle histories or the maximum execution time. A comprehensive tutorial document explaining the basic aspects of the MCNP code as an introduction for novice users is presented by J. K. Shultis and R. E. Faw in "*AN MCNP PRIMER*" [6].

The MCNPX input file given from previous STIP experiments has been modified according to STIP VI – Target 9 data. The surfaces and cells defining the lead target rods and specimen rods have been checked modifying some of them due to the new position in the target. The cells which are segmenting the SHT and the inverted BEW have been modified improving the old segmentation. A simulation has been also performed to calculate the cell volumes of each segmented region of the rods. These new volumes have been added to the MCNPX input file correcting the older ones. The material specification has been updated according to the newer materials filling the specimen rods. Finally, the proton beam implemented as a source for the MCNPX simulation has been calculated from the gamma mapping performed in STIP VI – Target 9 BEW.

The project is assessing the radiation damage in STIP VI – Target 9 by calculating the irradiation parameters of displacement per atom plus Helium and Hydrogen production in the specimen rods interspersed along Target 9. MCNPX code is used for implementing the model and calculating the proton and neutron fluence as well as the energy deposition in the target. The irradiation parameters of displacement per atom (dpa) plus Helium and Hydrogen concentration in atomic parts per million (appm) are computed in each specimen rod from the MCNPX simulation results. After the cool down of the irradiated SINQ Target, gamma-spectrometry measurements are performed on dosimetry discs to validate the results.

2. STIP VI – TARGET 9. CONFIGURATION

The MCNPX code has been used for implementing the model of STIP VI – Target 9. A schematic overview of the SINQ Target is presented in *Figure 2.1*. The proton beam injection is coming upwards and the neutron beams are extracted from the heavy water moderator tank surrounding the target.

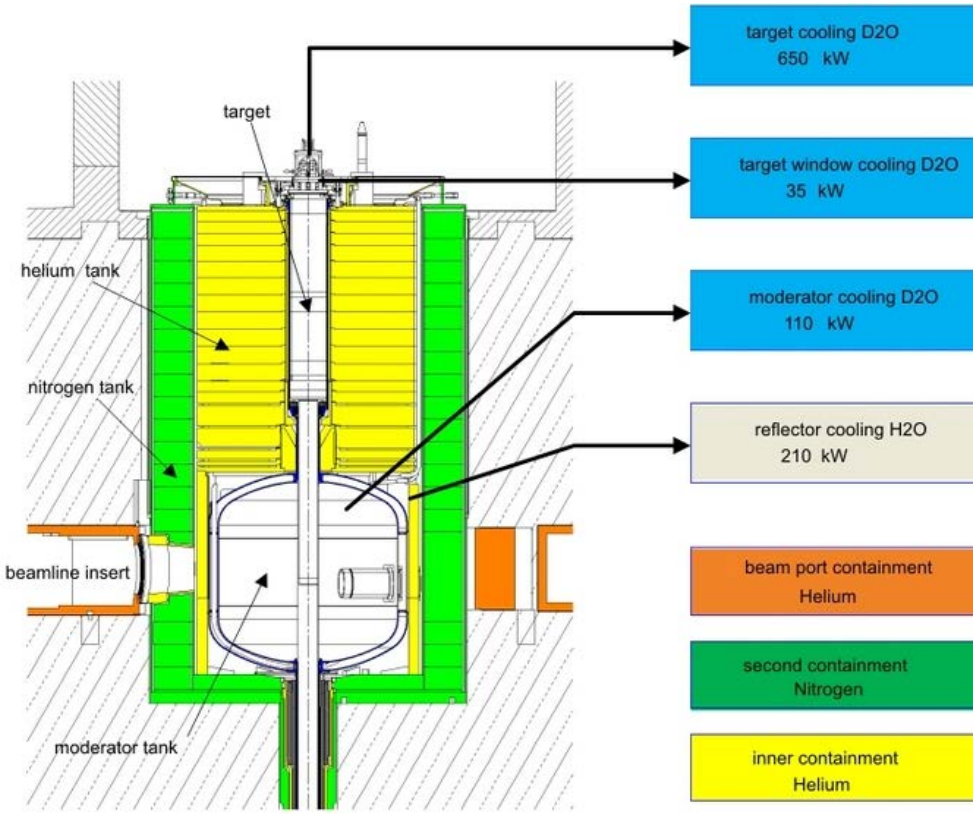

Figure 2.1 Schematic overview of the real SINQ Target [7]

The target implemented in the simulation model is just the lower part of the real target. It is mainly containing the target rod arrangement for producing neutrons and testing the different material rod samples. A schematic overview of the implemented SINQ Target is shown in *Figure 2.2*.

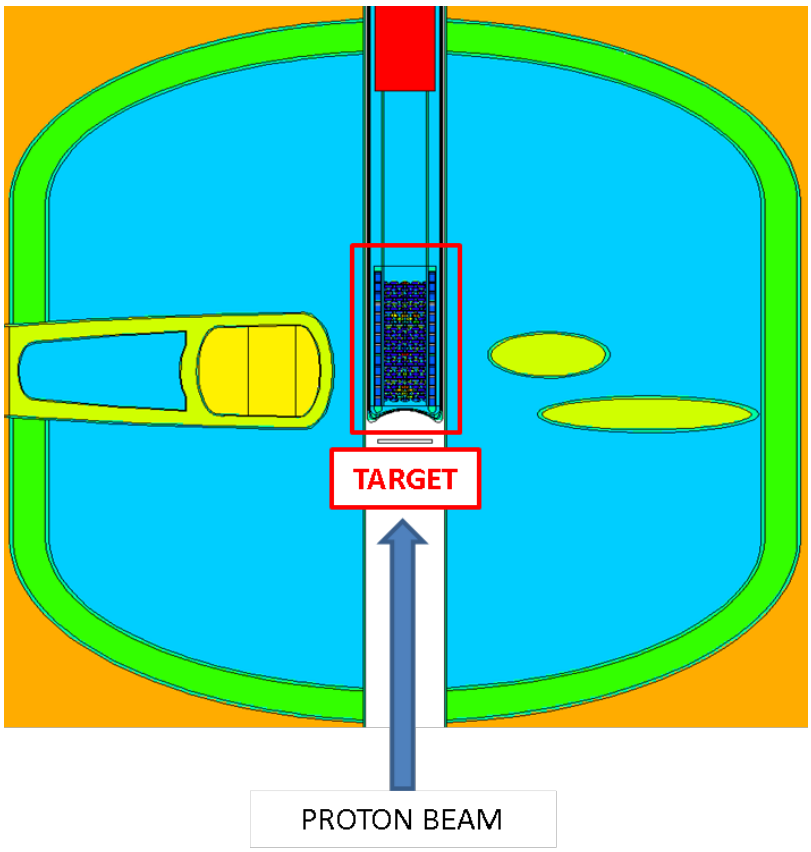

Figure 2.2 Overview of the implemented SINQ Target in MCNPX

The implemented target consists of double cylinder tubes, namely Safety Hull Tubes (SHT), linked to the bottom by an inverted hemisphere which stands for the inverted BEW, commonly named as Calotte.

The rods are placed in thirty-six rows along the Z-axis of an AlMg3 0.15 cm thick cylinder named as Rod Container Box (RCB). The outer diameter of the RCB is 12 cm. The lowest row (Row 0) is made of empty tubes in order to minimize the heat load in the region where the flow stabilizes. From Row 1 to Row 36, it is found the lead target rods and the interspersed specimen rods containing the material samples to be analyzed. The distance between rows is 1.011 cm and the distance from Row 0 to the bottom of the Rod Container Box is 1.96 cm. Heavy water is cooling the system by flowing inside the SHT and the RCB.

The overview of the implemented target with an XY top view of Row 36 is shown in next figure. The specimen rods interspersed along the target can be also seen due to the material code color.

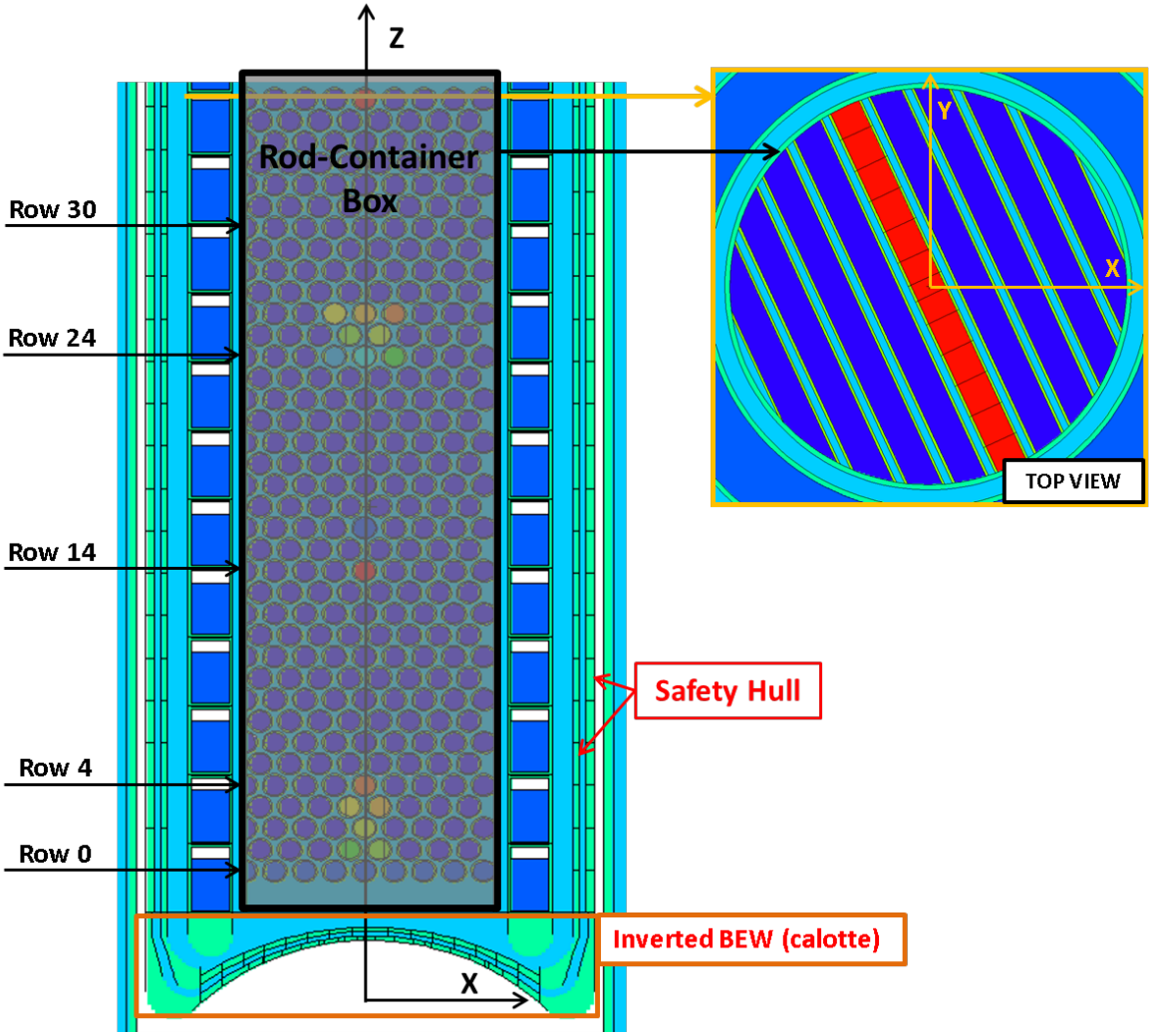

Figure 2.3 Overview of the implemented STIP VI – Target 9 in MCNPX

2.1 SAFETY HULL TUBE DESCRIPTION

The SHT is formed by two AlMg3 cylinder walls. The outer one has an average radius of 10.4 cm and a thickness of 0.4 cm. The inner one has an average radius of 9.75 cm and a thickness of 0.3 cm. The SHT walls have been segmented along Z-axis in fourteen cells for obtaining a Z-axis profile of proton and neutron fluences escaping from the target and its irradiation parameters. In the middle of the two cylinder walls, there is a 0.3 cm thick layer of heavy water for cooling purposes.

A zoom picture of the target is illustrated in *Figure 2.4* for showing the SHT implementation.

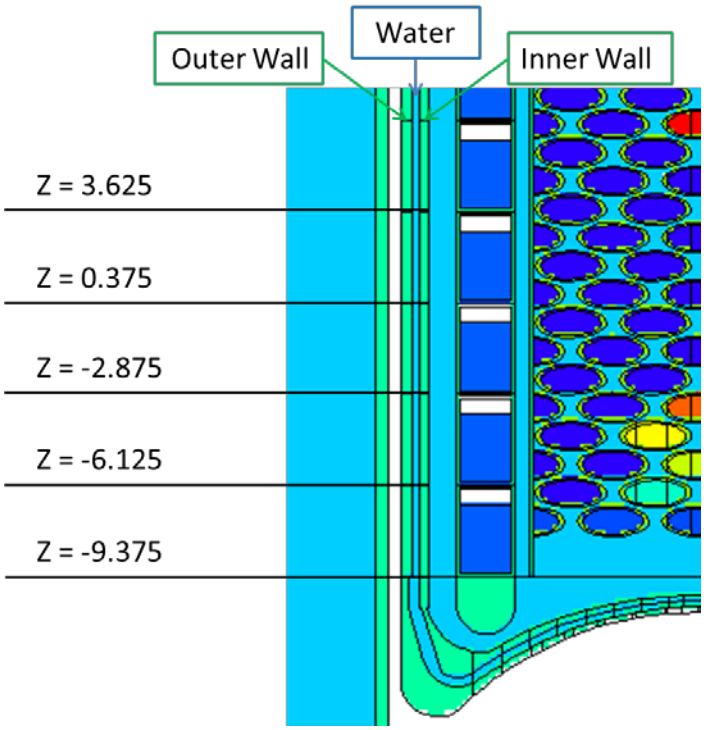

Figure 2.4 Overview of the implemented Safety Hull

2.2 CALOTTE DESCRIPTION

The Calotte is implemented through two spheres of 12.2 cm and 15.0 cm radius and a circular torus for linking itself with the SHT. It consists of three layers, the two outer are made of AlMg3 and the middle one is filled with heavy water for cooling. The first layer and the heavy water layer have a thickness of 0.4 cm. The proton beam is hitting the first layer which has been segmented by X and Y planes projecting a rectangular mesh. *Figure 2.5* is showing a picture of the implemented Calotte.

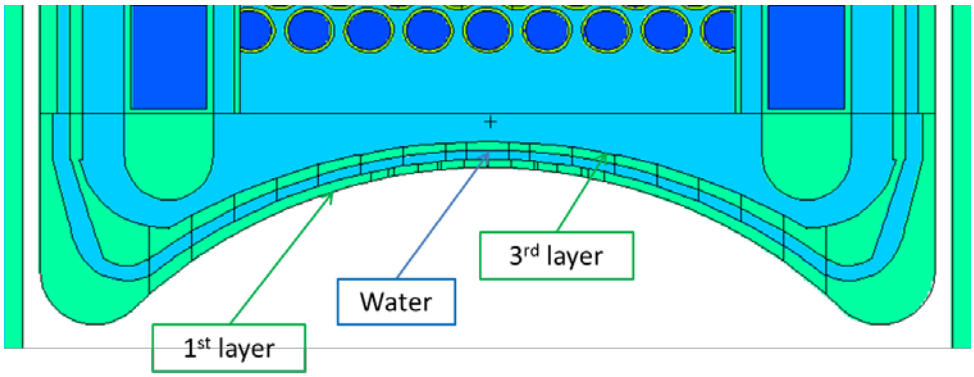

Figure 2.5 Overview of the implemented Calotte

2.3 ROD DESCRIPTION

The rods are placed in the RCB fitting thirty-six rows. The RCB is basically implemented by two cylinders 43.5 cm high with a radius of 5.85 and 6.00 cm. The first row, Row 0, is just consisting on zircaloy tubes filled with water. The rest of the rows are containing the specimen rods and the lead target rods for producing the spallation neutrons.

The lead target rods are implemented by an inner cylinder of 4.625 mm radius and surrounded by a zircaloy cladding of 5.375 mm radius. The specimen rods are mostly implemented in the same way but filled with test specimens. Four specimen rods (Rod 6, Rod 10, Rod 11 and Rod 12) are surrounded by a steel cladding being its inner and outer radius of 4.90 mm and 5.40 mm, respectively. The name and position of each specimen rod can be seen in *Figure 2.6*.

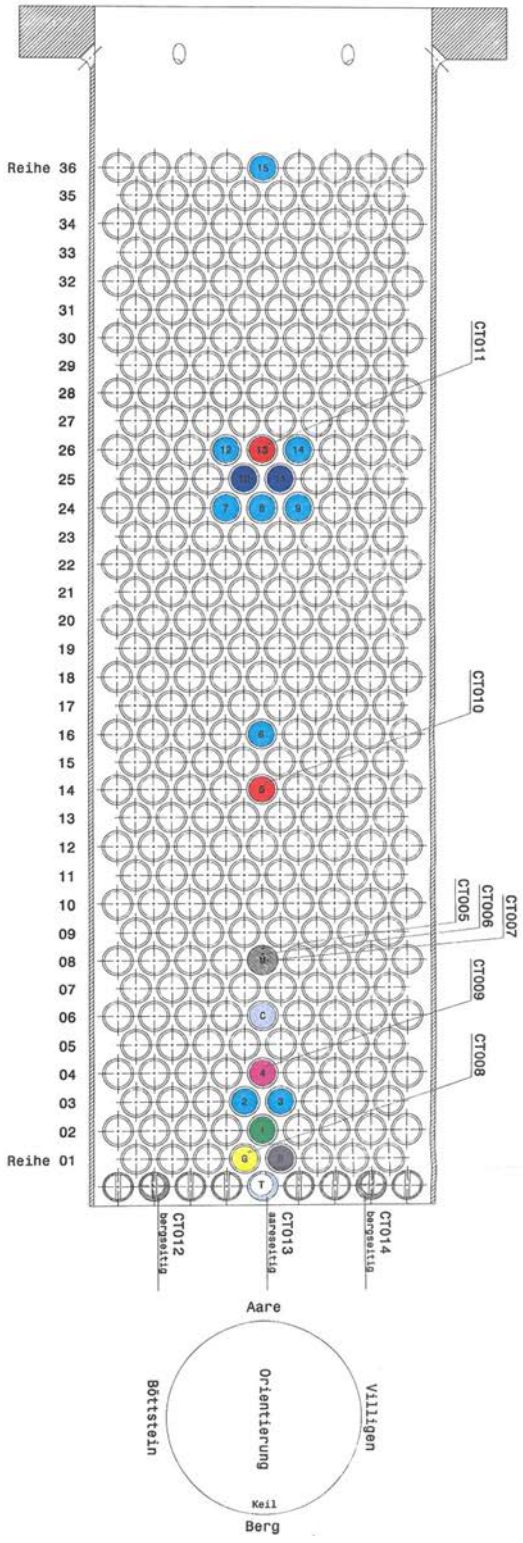

Figure 2.6 STIP VI – TARGET 9. Position of the specimen rods

All the center rods plus the specimen rods are segmented in thirteen cells for analyzing the fluence profile in the rod. The segmentation is done by cutting planes at 0.25, 1.0, 2.0, 3.0, 4.0 and 5.0 cm in the positive and negative side. The end cells are limited between the plane at 5.0 cm and the RCB. An XY top view of Row 26 containing Rod 12, Rod 13 and Rod 14 can be seen in *Figure 2.7*.

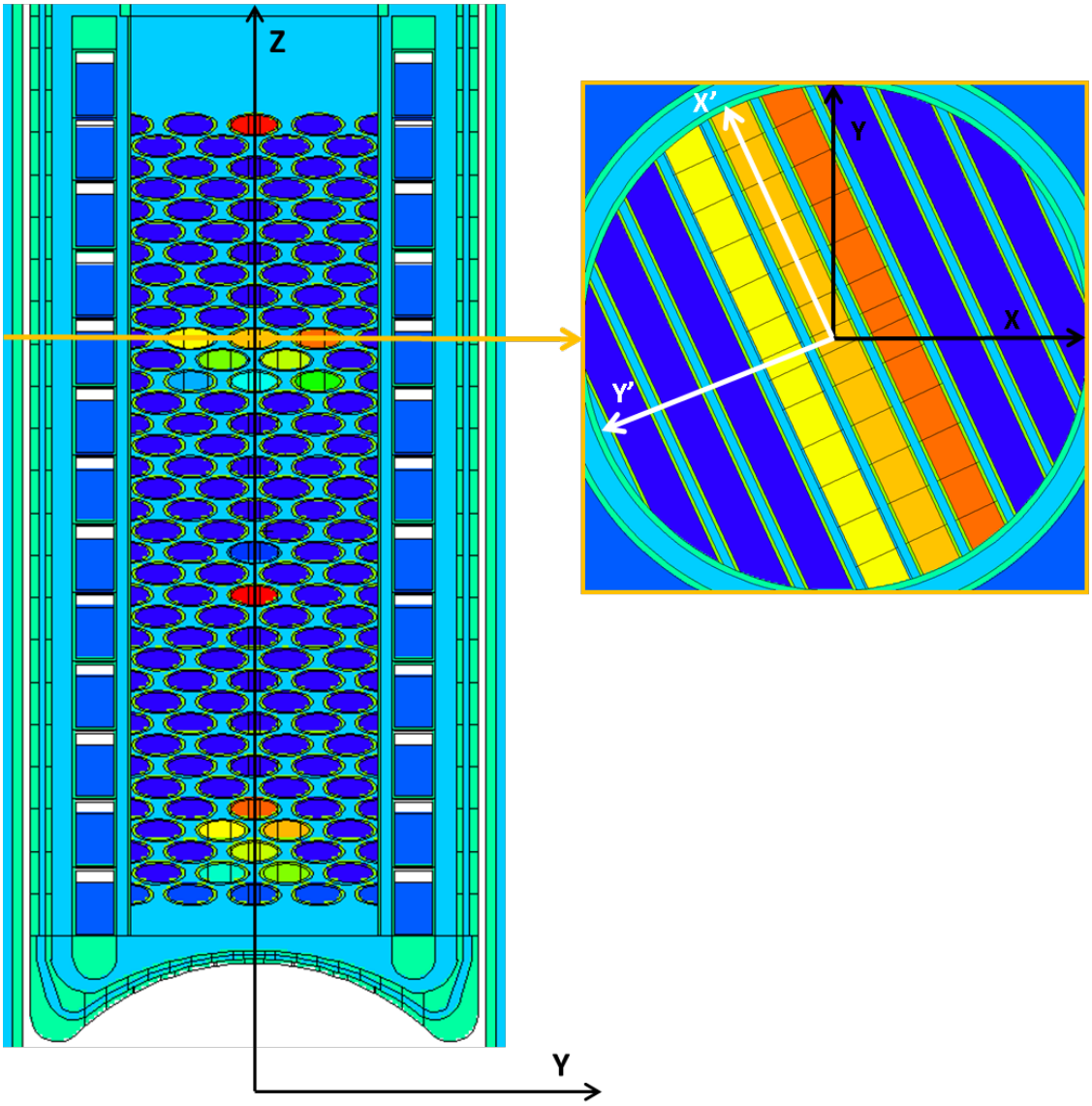

Figure 2.7 STIP VI – TARGET 9. Top view of Row 26

An example of the geometry and dimensions of a real specimen rod can be seen in *Figure 2.8*. The real configuration of the test sample rods consists of many specimens packed with some filler and fitting cylindrical tubes that are placed in the real specimen rod.

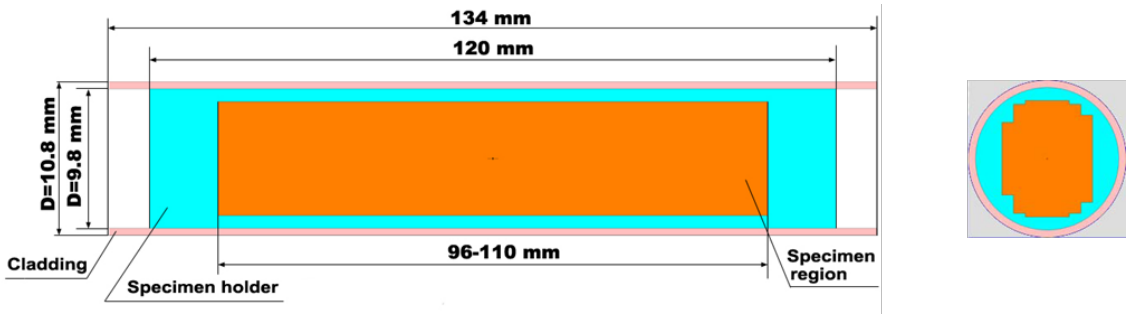

Figure 2.8 Geometry and dimensions of a specimen rod [8]

The typical specimens are Transmission Electron Microscopy (TEM) disk specimens, Large Tensile (LT) and Small Tensile (ST) specimens, Bend Bar (BB) and Charpy specimens. Most of them are made of austenitic and martensitic steels like SS316L, T91 or Eurofer97. As an example, *Figure 2.9* is showing a picture with the specimen rods used in STIP-II. There is also a sketch showing the dimension of STIP IV specimens in *Figure 2.10*.

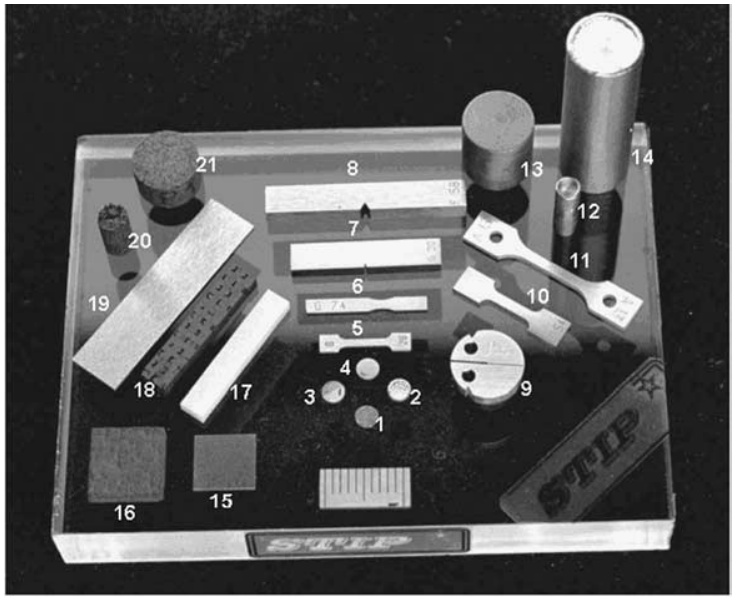

Figure 2.9 Common specimens used in STIP II [4]

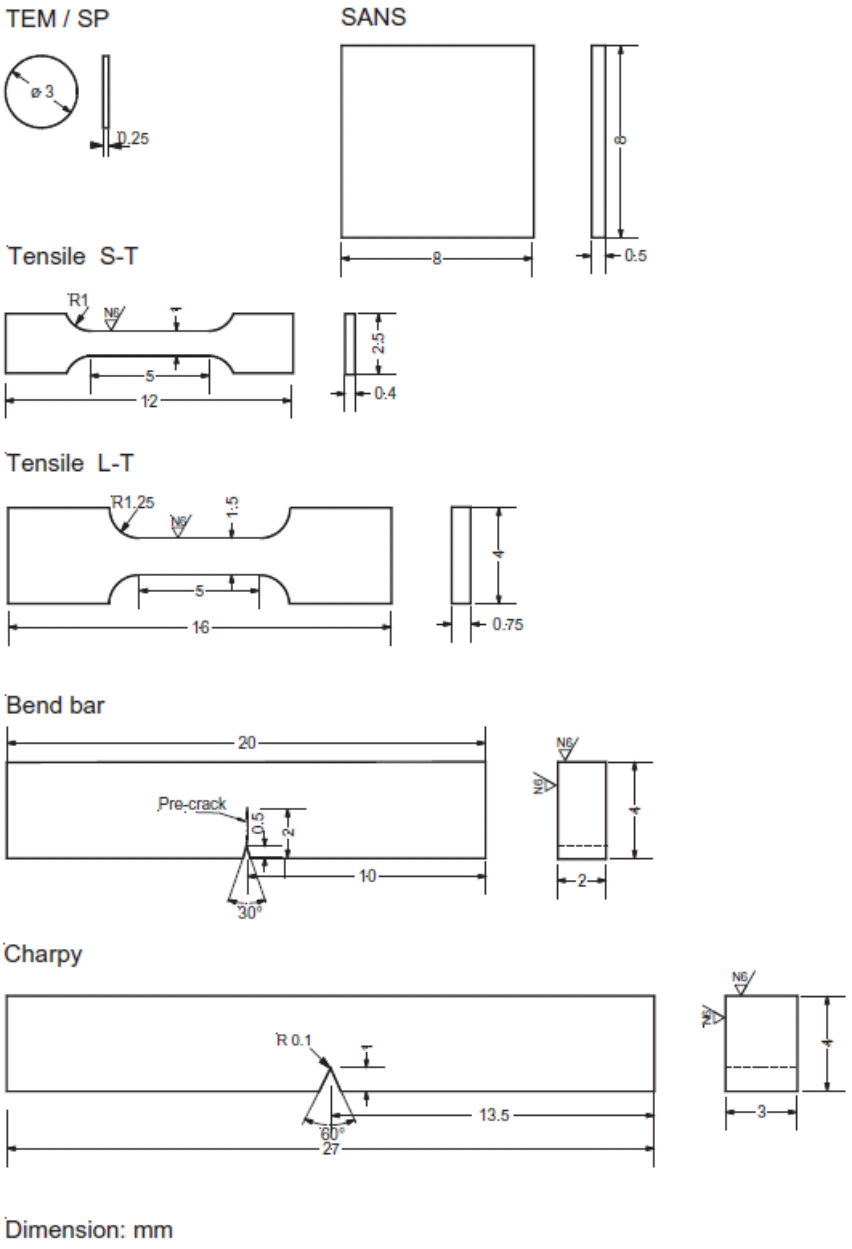

Figure 2.10 Sketch showing the dimensions of STIP IV specimens [9]

All these specimens have been implemented in the model considering a uniform distribution along the specimen rods for simplifying the simulation. The average composition has been implemented in the material card of the MCNPX input file by adding all natural isotopes that constitute the material with its corresponding weight fraction. The material data specification of each specimen rod is given in *Annex A. MATERIAL SPECIFICATION*.

2.4 CALOTTE GAMMA MAPPING

The source definition for the MCNPX simulation has been implemented from the gamma mapping performed at the irradiated AlMg3 Calotte of STIP VI – Target 9. A picture of the beam footprint found in the Calotte after irradiation is shown in *Figure 2.11*.

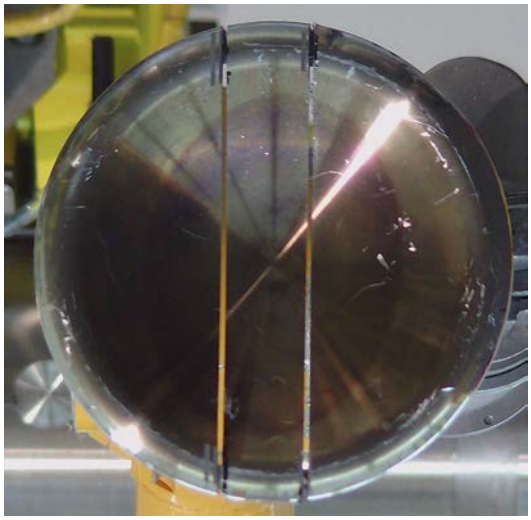

Figure 2.11 Proton beam footprint in the calotte

The gamma mapping is performed by measuring the Na-22 counts at the calotte fitting an XY plane of 160x160 mm^2, which is segmented in 4x4 mm^2 cells. *Figure 2.12* is showing this procedure of Na-22 measurement.

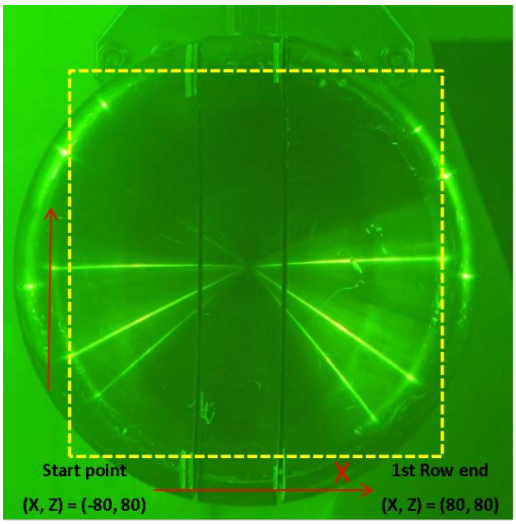

Figure 2.12 Gamma mapping performance in the calotte

The results obtained from the gamma mapping are used for calculating the proton fluence by applying some geometry corrections and convert factors. *Figure 2.13* shows the plotted results of the proton fluence distribution in STIP VI – Target 9.

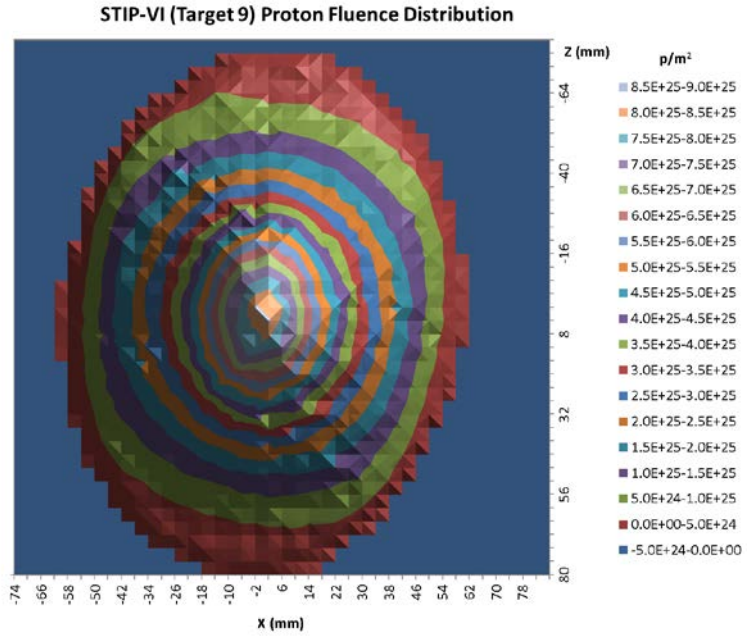

Figure 2.13 Results of the gamma mapping performed in STIP VI – Target 9

2.5 ADJUSTMENTS ON STIP VI MCNPX MODEL

The MCNPX input file given from previous STIP experiments has been modified according to STIP VI – Target 9 data. In this section, the main adjustments done in the MCNPX input file are briefly explained. As it has been mentioned before, the general structure of a MCNPX input file is divided in the following blocks: Cells and Surfaces (Geometry definition), Material definition, Source definition and Transport Parameters.

Geometry definition

The surfaces and cells defining the lead target rods and specimen rods have been checked modifying some of them due to the new position in the target, like the steel cladding specimen rods. A simulation has been also performed to calculate the cell volumes of each segmented region of the rods. These new volumes have been added to the MCNPX input file correcting the older ones. *Figure 2.14* is showing Rod 6 implementation in the MCNPX input file as an example of the adjustments done. The first number in each line is a unique number which identifies each cell implemented. The second number is referred to the material which is filling the cell and its density is shown as the third number in grams divided by cubic centimeters. The other numbers are identifying the surfaces used for generating the cell. The last number defines the volume of each cell, which helps MCNPX in case it cannot calculate the volume by itself.

```
c ROW 16, Position 5, STIP SAMPLES - STIP ROD 6
c
91601  38    -6.95100e+00   -20   -301 -700      vol=0.651411265
91602  38    -6.95100e+00   -20   -301 -701 700  vol=0.754296396
91603  38    -6.95100e+00   -20   -301 -702 701  vol=0.754296396
91604  38    -6.95100e+00   -20   -301 -703 702  vol=0.754296396
91605  38    -6.95100e+00   -20   -301 -704 703  vol=0.754296396
91606  38    -6.95100e+00   -20   -301 -705 704  vol=0.565722297
91607  38    -6.95100e+00   -20   -301 -706 705  vol=0.377148198
91608  38    -6.95100e+00   -20   -301 -707 706  vol=0.565722297
91609  38    -6.95100e+00   -20   -301 -708 707  vol=0.754296396
91610  38    -6.95100e+00   -20   -301 -709 708  vol=0.754296396
91611  38    -6.95100e+00   -20   -301 -710 709  vol=0.754296396
91612  38    -6.95100e+00   -20   -301 -711 710  vol=0.754296396
91613  38    -6.95100e+00   -20   -301  711      vol=0.651411265
c
c ROW 16, Position 5, STEEL TUBE - STIP ROD 6
c
91614   26    -7.85000e+00   -20    301  -302 -700      vol=0.1397237825
91615   26    -7.85000e+00   -20    301  -302 -701 700  vol=0.161792022
91616   26    -7.85000e+00   -20    301  -302 -702 701  vol=0.161792022
91617   26    -7.85000e+00   -20    301  -302 -703 702  vol=0.161792022
91618   26    -7.85000e+00   -20    301  -302 -704 703  vol=0.161792022
91619   26    -7.85000e+00   -20    301  -302 -705 704  vol=0.121344016
91620   26    -7.85000e+00   -20    301  -302 -706 705  vol=0.0808960108
91621   26    -7.85000e+00   -20    301  -302 -707 706  vol=0.121344016
91622   26    -7.85000e+00   -20    301  -302 -708 707  vol=0.161792022
91623   26    -7.85000e+00   -20    301  -302 -709 708  vol=0.161792022
91624   26    -7.85000e+00   -20    301  -302 -710 709  vol=0.161792022
91625   26    -7.85000e+00   -20    301  -302 -711 710  vol=0.161792022
91626   26    -7.85000e+00   -20    301  -302  711      vol=0.1397237825
```

Figure 2.14 Rod 6, cell implementation in the MCNPX input file

Figure 2.15 is showing the surfaces used for generating the cells which are defining Rod 6. There is also a first unique number identifying the surface which is followed by the characterization of each surface. The surfaces used for implementing the cells are Rectangular Parallelepiped (rcc), Cylinder parallel to X-axis (c/x) and Plane normal to X-axis (px). The number which is in the middle between the identifier number and the surface is related with the transformation applied to the surface.

```
c
19  1  rcc  0.0  0.0  -11.0  0.0  0.0  43.5  6.00
20  1  rcc  0.0  0.0  -11.0  0.0  0.0  43.5  5.85
c
c ************************************************************
c            SURFACES BY ROWS      (adjust SX TY)
c ************************************************************
c
c ROW 16 **STEEL ROD 6 Surfaces 301-302**
c
299   1   c/x  -1.27500e+00    7.13600e+00    4.62500e-01
300   1   c/x  -1.27500e+00    7.13600e+00    5.37500e-01
301   1   c/x   0.00000e+00    7.13600e+00    4.90000e-01
302   1   c/x   0.00000e+00    7.13600e+00    5.40000e-01
303   1   c/x   1.27500e+00    7.13600e+00    4.62500e-01
304   1   c/x   1.27500e+00    7.13600e+00    5.37500e-01
c
c segmenting surfaces
c
700  1    px   -5.0
701  1    px   -4.0
702  1    px   -3.0
703  1    px   -2.0
704  1    px   -1.0
705  1    px   -0.25
706  1    px    0.25
707  1    px    1.0
708  1    px    2.0
709  1    px    3.0
710  1    px    4.0
711  1    px    5.0
c
```

Figure 2.15 Rod 6, surface implementation in the MCNPX input file

The last adjustment done in the Geometry definition is referred to cells which are segmenting the SHT and the Calotte. These cells have been modified improving the old segmentation. Newer surfaces have been defined as well as cells for implementing the new segmentation. Basically, plane surfaces have been defined to reduce the segmentation step for providing more data in the region of interest.

Material definition

The material specification has been updated according to newer materials filling the specimen rods. *Figure 2.16* is showing the first lines of the material definition for number 38 which is filling Rod 6. The first number refers to the material and the designation of its particular cross section compilation. The number is specified as ZZZAAA.nnX which stands for the atomic number (ZZZ), the atomic mass number (AAA), the library identifier (nn) and the class of data (X). The second number is defining the weight fraction of each element.

```
c ---------------------------------------------------------
c   Material 38 for ROD 6 Density 6.951 g/cc
c ---------------------------------------------------------
m38       6012 -7.43770174E-04 &
          6013 -8.04441612E-06 &
         14028.70c -2.94946010E-03 &
         14029.70c -1.49766415E-04 &
         14030.70c -9.87271262E-05 &
         16032.70c -3.90651171E-05 &
         16033.70c -3.12751385E-07 &
         16034.70c -1.76539926E-06 &
         16036.70c -8.23029960E-09 &
         22046.70c -1.69749929E-06 &
         22047.70c -1.53083573E-06 &
         22048.70c -1.51684422E-05 &
         22049.70c -1.11314802E-06 &
         22050.70c -1.06582380E-06 &
         23050 -3.60075608E-06 &
         23051 -1.43670167E-03 &
         24050.70c -4.65546288E-03 &
         24052.70c -8.97759676E-02 &
         24053.70c -1.01798741E-02 &
         24054.70c -2.53398612E-03 &
         25055.70c -1.14898574E-02 &
         26054.70c -4.64014645E-02 &
         26056.70c -7.28403760E-01 &
         26057.70c -1.68220194E-02 &
         26058.70c -2.23870197E-03 &
```

Figure 2.16 Material definition of Number 38 (first lines)

Source definition

The source definition has been implemented like a segmented plane where each region is emitting upwards the proton fluence average calculated from the gamma mapping performed at the irradiated target. The first lines of the source definition implemented in MCNPX are shown in next figure.

```
c ***************************************************************************
sdef  x=d1 y=fx d2 z=-30. erg=575 vec=0 0 1 dir=1 par=9 tr=3
si1      -7.6   -7.2   -6.8   -6.4   -6.0   -5.6   -5.2   -4.8   -4.4   -4.0 &
         -3.6   -3.2   -2.8   -2.4   -2.0   -1.6   -1.2   -0.8   -0.4    0.0 &
          0.4    0.8    1.2    1.6    2.0    2.4    2.8    3.2    3.6    4.0 &
          4.4    4.8    5.2    5.6    6.0    6.4    6.8    7.2    7.6
sp1      0.00 1.64E+25 3.31E+25 5.16E+25 7.98E+25 1.15E+26 1.55E+26 2.04E+26 &
         2.69E+26 3.39E+26 4.19E+26 4.99E+26 6.00E+26 6.89E+26 7.93E+26 &
         8.84E+26 9.64E+26 1.03E+27 1.07E+27 1.11E+27 1.11E+27 1.08E+27 &
         1.03E+27 9.64E+26 8.71E+26 7.74E+26 6.77E+26 5.92E+26 4.88E+26 &
         4.04E+26 3.22E+26 2.62E+26 1.96E+26 1.48E+26 1.02E+26 7.31E+25 &
         4.51E+25 2.83E+25 1.16E+25
ds2  q   -7.2 11 -6.8 12 -6.4 13 -6.0 14 -5.6 15 -5.2 16 &
         -4.8 17 -4.4 18 -4.0 19 -3.6 20 -3.2 21 -2.8 22 &
         -2.4 23 -2.0 24 -1.6 25 -1.2 26 -0.8 27 -0.4 28 &
          0.0 29  0.4 30  0.8 31  1.2 32  1.6 33  2.0 34 &
          2.4 35  2.8 36  3.2 37  3.6 38  4.0 39  4.4 40 &
          4.8 41  5.2 42  5.6 43  6.0 44  6.4 45  6.8 46 &
          7.2 47  7.6 48
si11    -5.8 -5.4 -5.0 -4.6 -4.2 -3.8 -3.4 -3.0 -2.6 -2.2 &
        -1.8 -1.4 -1.0  -.6  -.2   .2   .6  1.0  1.4  1.8 &
         2.2  2.6  3.0  3.4  3.8  4.2  4.6  5.0  5.4  5.8
sp11     0.00E+000 0.00E+000 0.00E+000 0.00E+000 0.00E+000 0.00E+000 &
         0.00E+000 0.00E+000 0.00E+000 0.00E+000 1.14E+024 1.67E+024 &
         2.62E+024 2.60E+024 2.25E+024 2.19E+024 2.49E+024 1.39E+024 &
         0.00E+000 0.00E+000 0.00E+000 0.00E+000 0.00E+000 0.00E+000 &
         0.00E+000 0.00E+000 0.00E+000 0.00E+000 0.00E+000 0.00E+000
si12    -5.8 -5.4 -5.0 -4.6 -4.2 -3.8 -3.4 -3.0 -2.6 -2.2 &
```

Figure 2.17 Source definition implemented in MCNPX from the g-mapping

3. STIP VI – TARGET 9. SIMULATION RESULTS

Three tallies have been requested in the MCNPX simulation. The first two tallies are the proton and neutron averaged fluence over all cells of interest which, basically, are the ones belonging to the rods, the calotte, and the SHT. The other tally requested is the averaged Energy Deposition. A tally mesh has been also implemented for plotting the proton beam footprint and the proton and neutron fluence behavior over the entire target.

The proton and neutron fluences obtained in the MCNPX output file are expressed in neutrons or protons divided by square centimeters normalized to one source particle. In order to obtain the fluence in neutrons or protons divided by square meters, it has been multiplied by the inverse of the electron elementary charge ($1.6 \cdot 10^{-19}$ C), the STIP VI total irradiation (13.16 Ah) and the corresponding unit converter factors. The procedure followed for neutrons is presented next:

$$\frac{neutrons}{cm^2 \cdot \text{particles}} \cdot \frac{1}{1.6 \cdot 10^{-19} As} \cdot 13.16\, Ah \cdot \frac{3600\, s}{1\, h} \cdot \frac{10000\, cm^2}{1\, m^2} = 2.96 \cdot 10^{+27}\ \frac{neutrons}{m^2} \qquad (1)$$

The proton and neutron fluences as well as the energy deposition that have been obtained from the MCNPX simulation in the different regions of interest is presented in the following sections.

3.1 PROTON FLUENCE IN THE CALOTTE

The proton fluence values obtained at the center of the calotte are presented in *Figure 3.1* by representing an XY plane. The maximum proton fluence at the calotte is 8.27×10^{25} p/m^2.

Y \ X (cm)	-1.50	-0.75	-0.25	0.25	0.75	1.50
1.75	5.02E+25	5.62E+25	5.76E+25	5.93E+25	5.66E+25	5.00E+25
1.25	5.97E+25	6.52E+25	6.87E+25	6.97E+25	6.78E+25	5.85E+25
0.75	6.73E+25	7.47E+25	7.80E+25	7.83E+25	7.59E+25	6.69E+25
0.25	6.91E+25	7.91E+25	8.27E+25	8.27E+25	8.08E+25	6.86E+25
-0.25	6.61E+25	7.49E+25	7.95E+25	7.84E+25	7.76E+25	6.86E+25
-0.75	6.03E+25	7.01E+25	7.34E+25	7.35E+25	7.15E+25	6.39E+25
-1.25	5.01E+25	5.56E+25	5.89E+25	6.07E+25	5.83E+25	5.10E+25
-1.75	4.07E+25	4.51E+25	4.88E+25	4.91E+25	4.66E+25	4.19E+25

Figure 3.1 Proton fluence in the calotte (p/m^2)

The proton fluence obtained from the gamma mapping at the center of the irradiated calotte is also presented in *Figure 3.2*. The maximum proton fluence of the gamma mapping is 8.59×10^{25} p/m^2.

Y \ X (cm)	-1.40	-1.00	-0.60	-0.20	0.20	0.60	1.00	1.40
1.60	5.29E+25	5.93E+25	6.72E+25	6.89E+25	7.13E+25	7.24E+25	6.29E+25	5.35E+25
1.20	5.71E+25	6.60E+25	7.43E+25	7.61E+25	7.90E+25	7.41E+25	6.70E+25	5.85E+25
0.80	6.09E+25	7.09E+25	7.46E+25	8.13E+25	7.88E+25	7.74E+25	6.96E+25	6.06E+25
0.40	6.15E+25	7.12E+25	7.84E+25	8.58E+25	8.17E+25	7.61E+25	7.20E+25	6.27E+25
0.00	6.22E+25	7.13E+25	8.08E+25	8.25E+25	8.59E+25	7.60E+25	7.20E+25	6.24E+25
-0.40	5.85E+25	6.85E+25	7.37E+25	8.18E+25	7.99E+25	7.38E+25	6.98E+25	5.85E+25
-0.80	5.81E+25	6.73E+25	7.41E+25	7.72E+25	7.48E+25	7.22E+25	6.57E+25	5.69E+25
-1.20	5.34E+25	6.14E+25	6.67E+25	7.08E+25	6.87E+25	6.76E+25	5.99E+25	5.30E+25
-1.60	4.95E+25	5.72E+25	5.98E+25	6.55E+25	6.18E+25	6.00E+25	5.48E+25	4.78E+25

Figure 3.2 Proton fluence obtained from the gamma mapping (p/m^2)

Although it is quite complicated to compare these fluence values, a slightly higher proton fluence values is observed in the positive side of the Y-axis, close to the center. The fact is that the real proton beam is hitting the calotte with a deviation of around 2 mm in the positive side of the Y-axis.

The top and bottom view of the proton beam footprint in the target is compared with the real configuration in order to validate the results and the correct implementation of the source definition. *Figure 3.3* is showing the implemented proton beam footprint and *Figure 3.4* is showing the real proton beam footprint and its orientation.

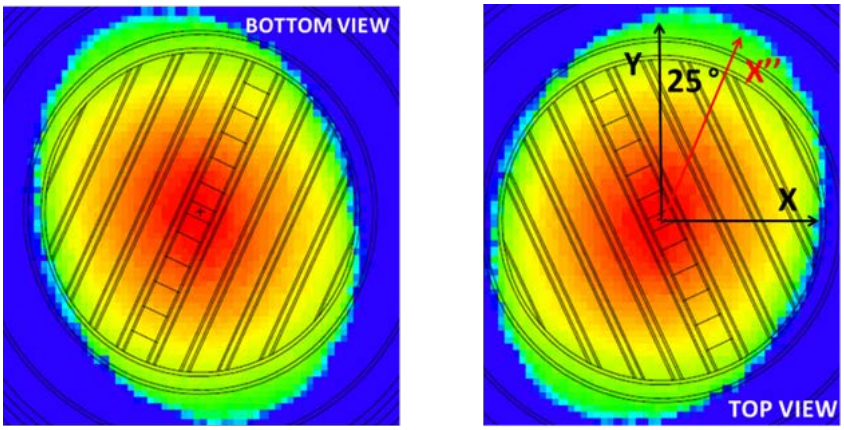

Figure 3.3 Top/Bottom view of the implemented proton beam footprint

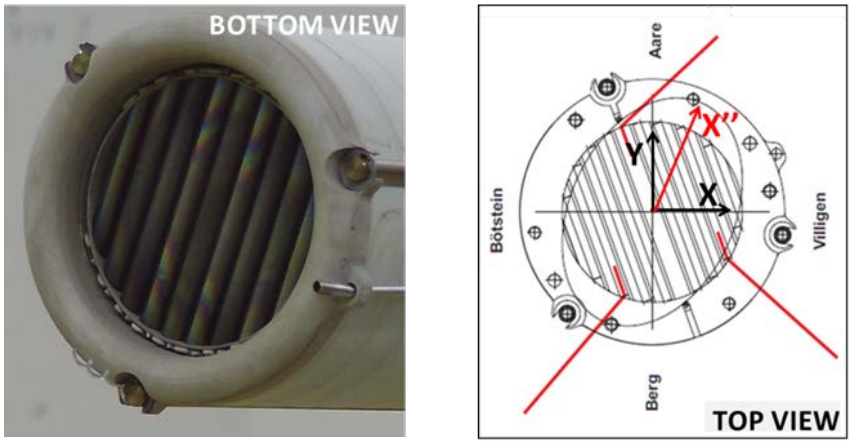

Figure 3.4 Real footprint in the calotte with the orientation

The proton beam footprint simulated adequately fits the real configuration with the expected 25º angle of deviation. It verifies the correct implementation of the proton beam profile in the MCNPX model.

3.2 PROTON AND NEUTRON FLUENCE DISTRIBUTION

The proton and neutron fluence distribution over the target is presented in *Figure 3.5*. The expected behavior is obtained in both cases. The proton beam is hitting the center of the calotte and first row, Row 0, without any significant reduction on its fluence. Although it is not clearly seen, the proton fluence is decreasing progressively along the target after Row 1 due to their loss of energy in scattering interactions.

The maximum neutron fluence is obtained between Row 5 and Row 10. In Row 1, where the first lead target rods are placed, spallation reactions start to be produced increasing the neutron fluence till its maximum. After that, the neutron fluence is also decreasing progressively because of the lower energy of the protons which induces less spallation reactions.

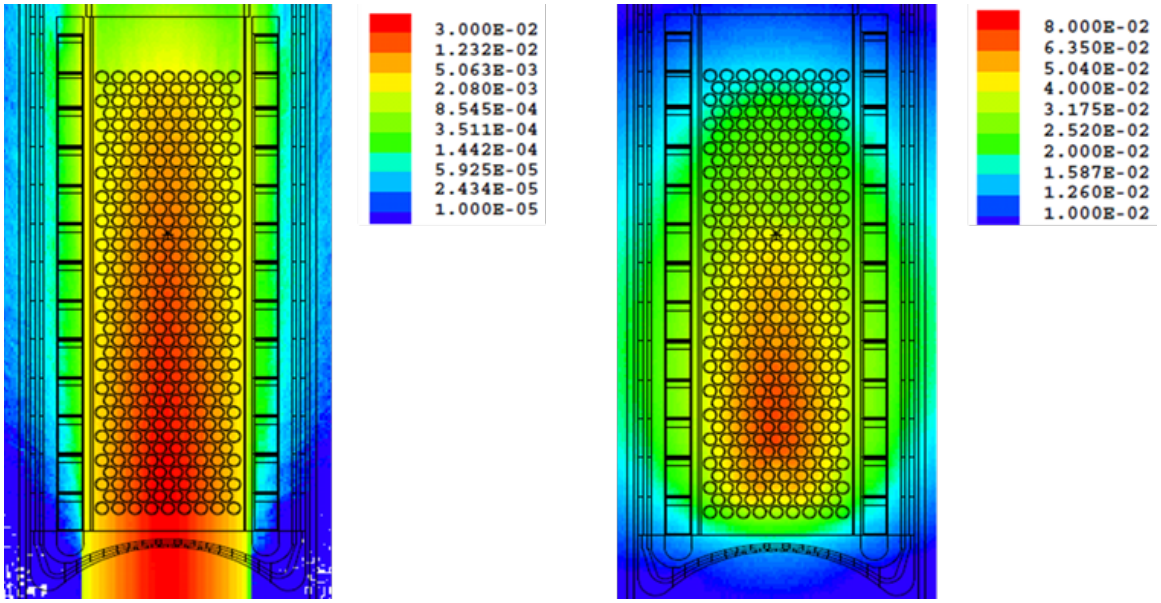

Figure 3.5 Proton and Neutron fluence distribution over the target (Normalized to one source particle)

3.3 PROTON FLUENCE IN THE RODS

The proton fluence over the central rods of the target is plotted in *Figure 3.6*. The central rods of the target are those ones placed in the center of the even rows. The proton fluence distribution is decreasing progressively along the further rows of the target. The differences between the proton fluence at each row can be seen clearly.

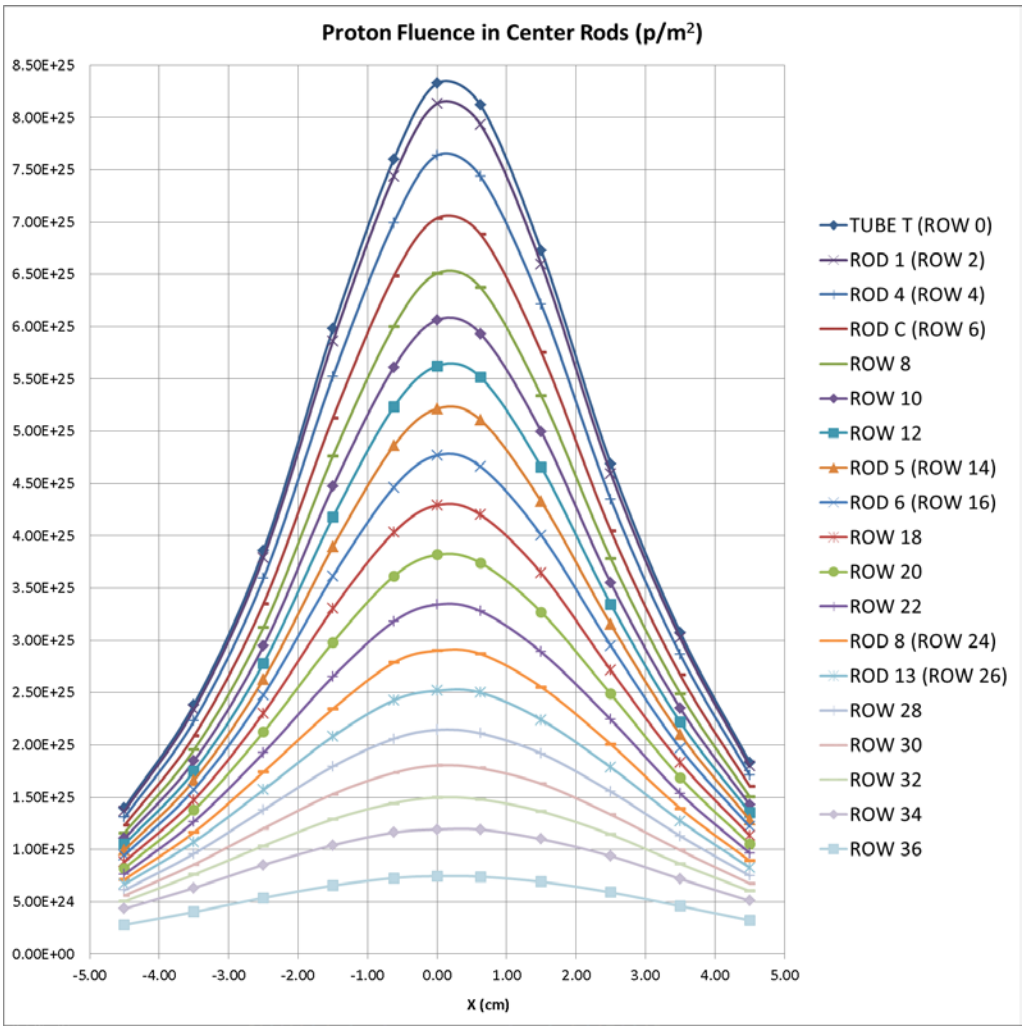

Figure 3.6 Proton fluence in the center rods

The maximum proton fluence is obtained at Tube T (Row 0) and it decreases progressively along the further central rows due to the proton loss of energy in scattering interactions. There are two important points to highlight. The first one is related with the proton fluence peak obtained in all central rods which is a bit displaced to the right side due to the proton beam shift.

The second point is found looking at the small difference between the proton fluence peak of Tube T (Row 0) and Rod 1 (Row 2) in comparison with the bigger differences between further rods. It is caused because Row 0 is just formed by zircaloy tubes filled with water. So, the proton fluence is just slightly scattered at Row 0.

The proton fluence behavior in the specimen rods is shown in *Figure 3.7*. The behavior is quite similar as the observed for the central rods but it is interesting to analyze the behavior between rods placed in the same row.

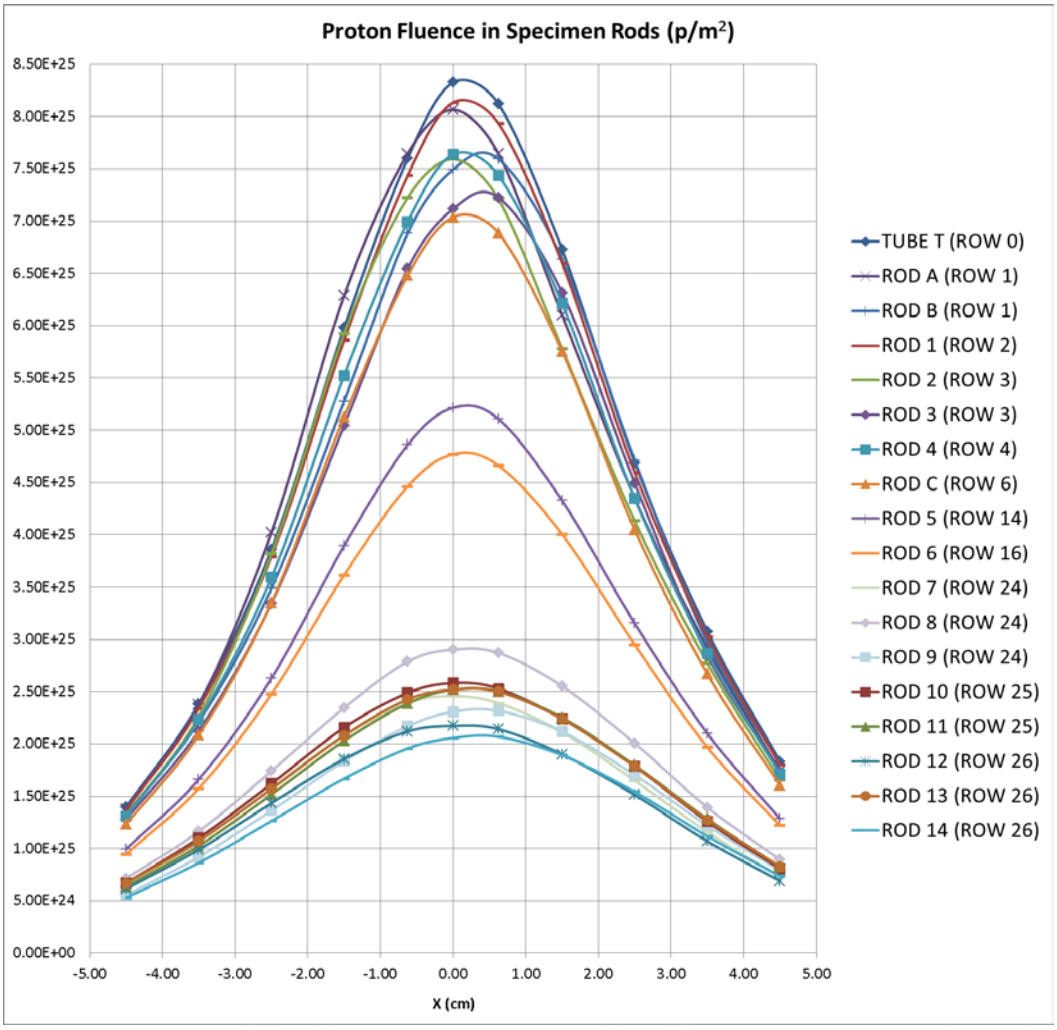

Figure 3.7 Proton fluence in the specimen rods

In the lower part of the target, Rod A (left side) and Rod B (right side) are placed in Row 1, and Rod 2 (left side) and Rod 3 (right side) in Row 3. The rods placed in the left side have a higher proton fluence peak which is obtained in the center of the rod. However, the rods placed in the right side have a lower proton fluence peak than the left side rods and it is obtained at X = 0.7 cm, approximately. The explanation of that fact is found in the deviation of the proton beam. *Figure 3.8* is showing the proton fluence of Rod A and Rod B to see clearly this behavior.

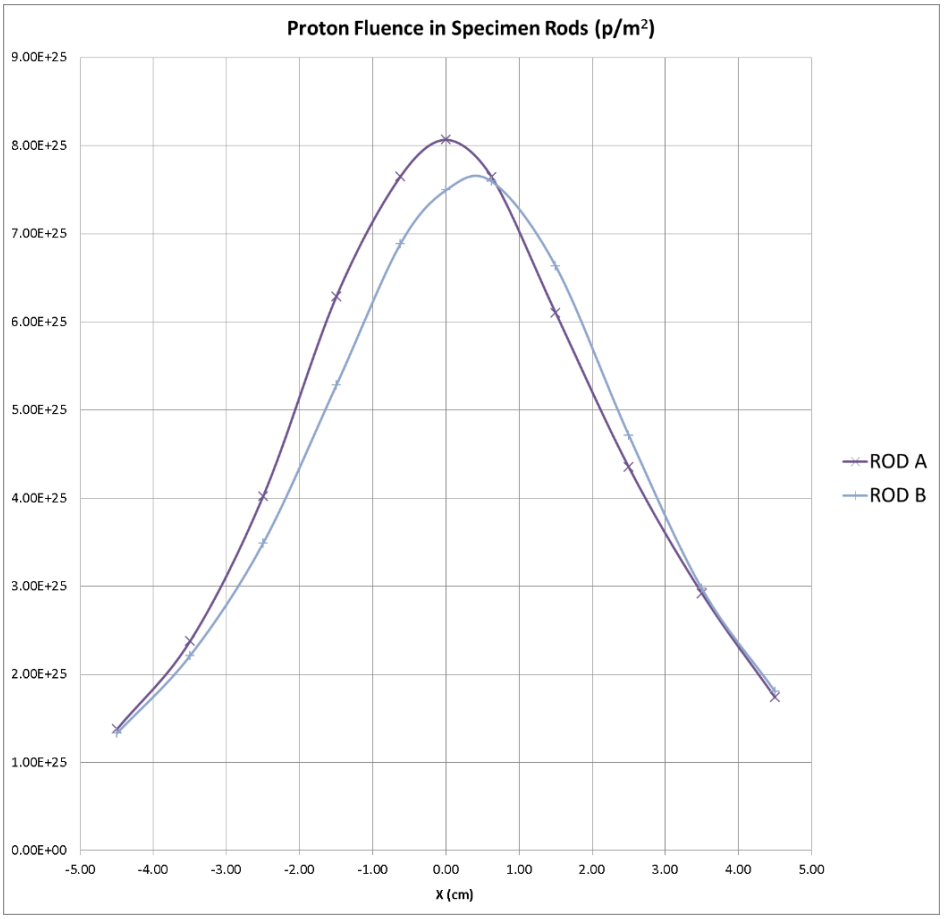

Figure 3.8 Proton fluence in Rod A and Rod B

Figure 3.9 is showing a top view of the row where Rod A and Rod B are placed. As the proton beam is shifted a few millimeters, there is a higher proton fluence in the positive side of the Y'' axis of the beam footprint near the center. Assuming that and looking at the picture, it is clear that the proton fluence is higher in the center of Rod A than in Rod B because the maximum proton fluence, due to the deviation, is closer to Rod A center. It also explains the peak displacement to the positive X'-rod-axis for the central rods.

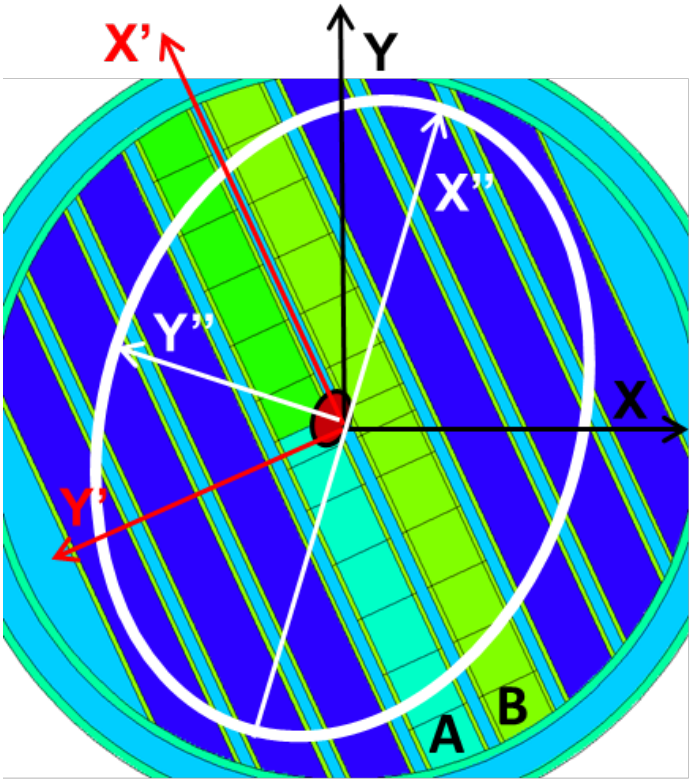

Figure 3.9 Top view of the target at Row 1: Rod A and Rod B

Another interesting point is comparing the maximum proton fluence of Rod 1 (Row 2) and Rod 4 (Row 4) against Rod A&B (Row 1) and Rod 2&3 (Row 3), respectively. Although the proton fluence is decreasing progressively along the target, Rod 1 (Row 2) has a higher maximum proton fluence than Rod A&B (Row 1). The same is occurring for Rod 4 (Row 4) in comparison with Rod 2&3 (Row 3). This phenomenon is explained by the lower gain of protons due to its geometrical position in the target and the lower fluence arriving to the rods not placed in the center because of the proton beam implemented which is also decreasing axially. *Figure 3.10* is showing the proton fluence in the specimen rods located at the lower part of the target.

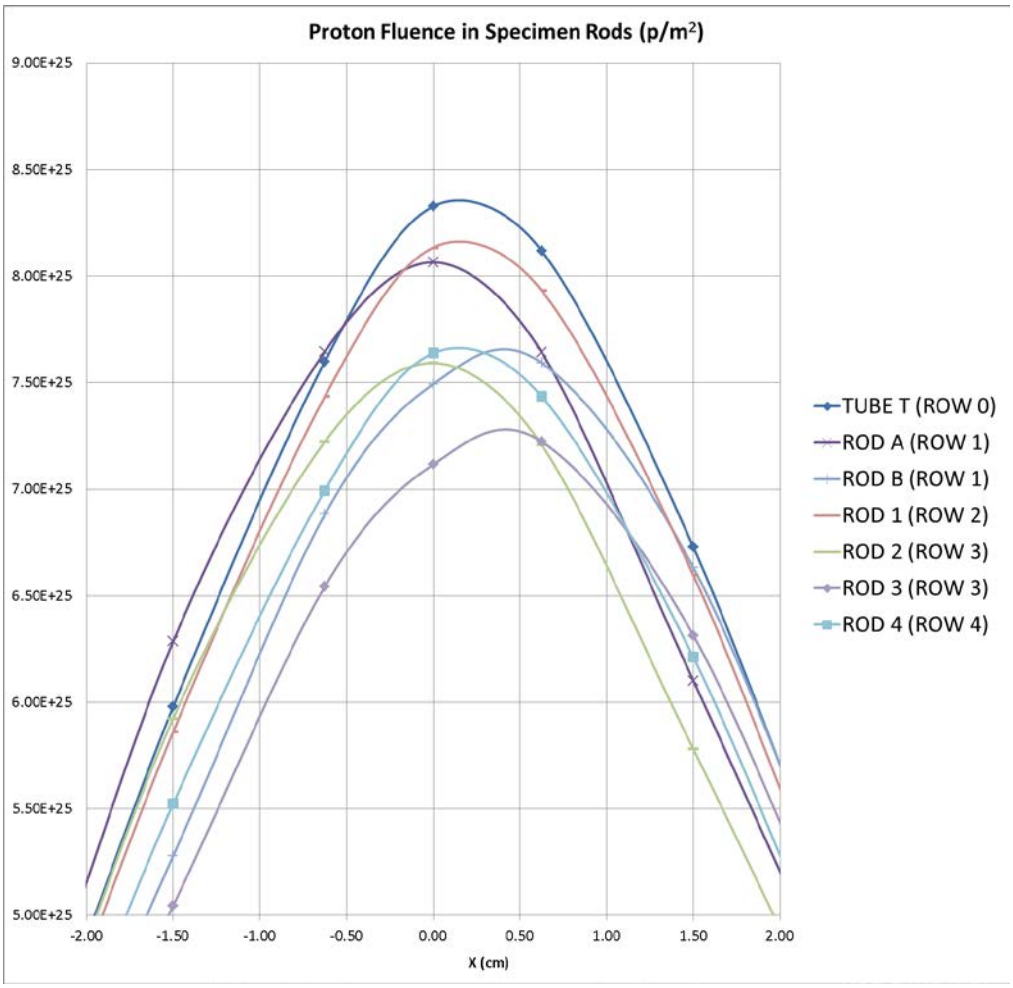

Figure 3.10 Proton fluence in the lower part of the target

All these phenomena are also found in the upper part of the target. *Figure 3.11* is showing the proton fluence in the specimen rods placed in the upper part of the target. Rod 7, Rod 8 and Rod 9 are placed in Row 24. Rod 8 has a higher proton fluence than Rod 7&9 because it is a center rod and Rod 7 has a higher proton fluence than Rod 9 because Rod 7 is placed in the left side. Although the same behavior is found in the lower part of the target, the differences between the proton fluence in the upper part of the target are much smaller because the proton fluence is lower and better distributed along the target.

These phenomena are also occurring in Row 26 where Rod 12 (left), Rod 13 (center) and Rod 14 (right) are placed. The proton fluence in Row 25 (Rod 10 and Rod 11) is higher than Rod 7 and Rod 9 (Row 24) due to the geometrical position because Rod 7 and Rod 9 are further from the center than Rod 10 and Rod 11.

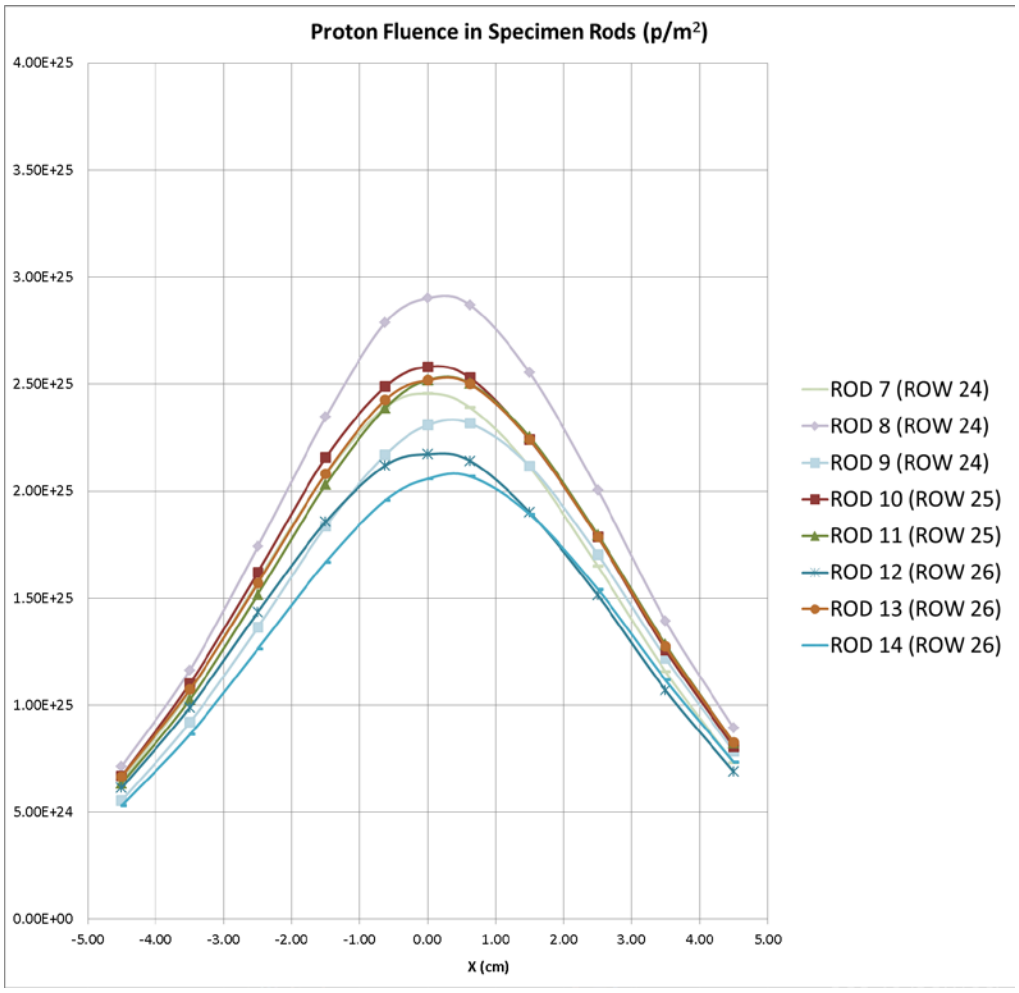

Figure 3.11 Proton fluence in the upper part of the target

Finally, *Figure 3.12* and *Figure 3.13* are showing the proton energy spectrum at the center of the specimen rods placed in the lower and upper part of the target. The proton energy is decreasing along the target due to scattering becoming in less proton fluence. The proton energy range in the lower, medium and upper part of the target is clearly identified, becoming approximately in 500-575 MeV, 375-450 MeV and 225-350 MeV, respectively.

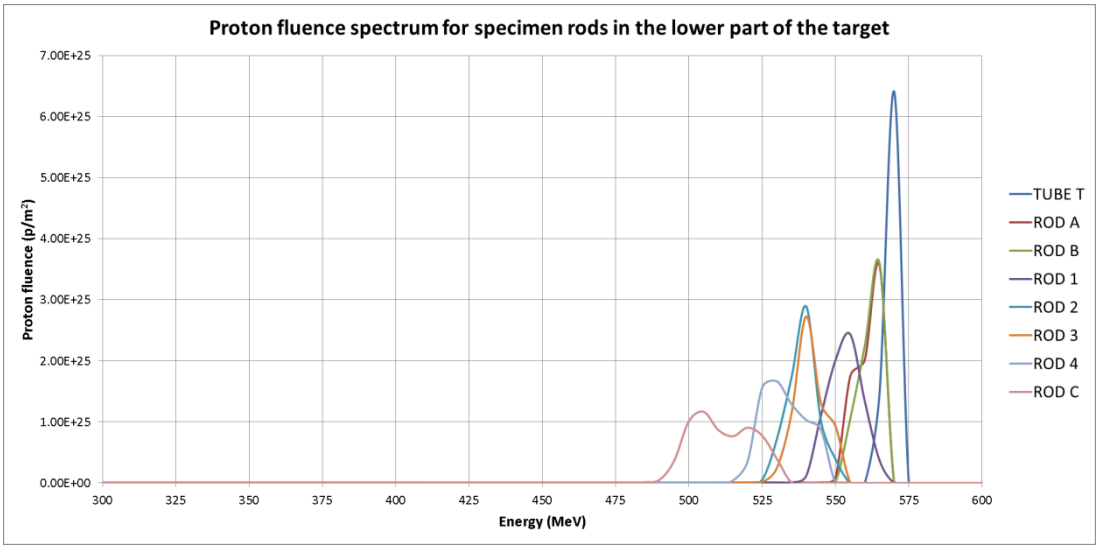

Figure 3.12 Proton fluence spectrum for specimen rods (lower target)

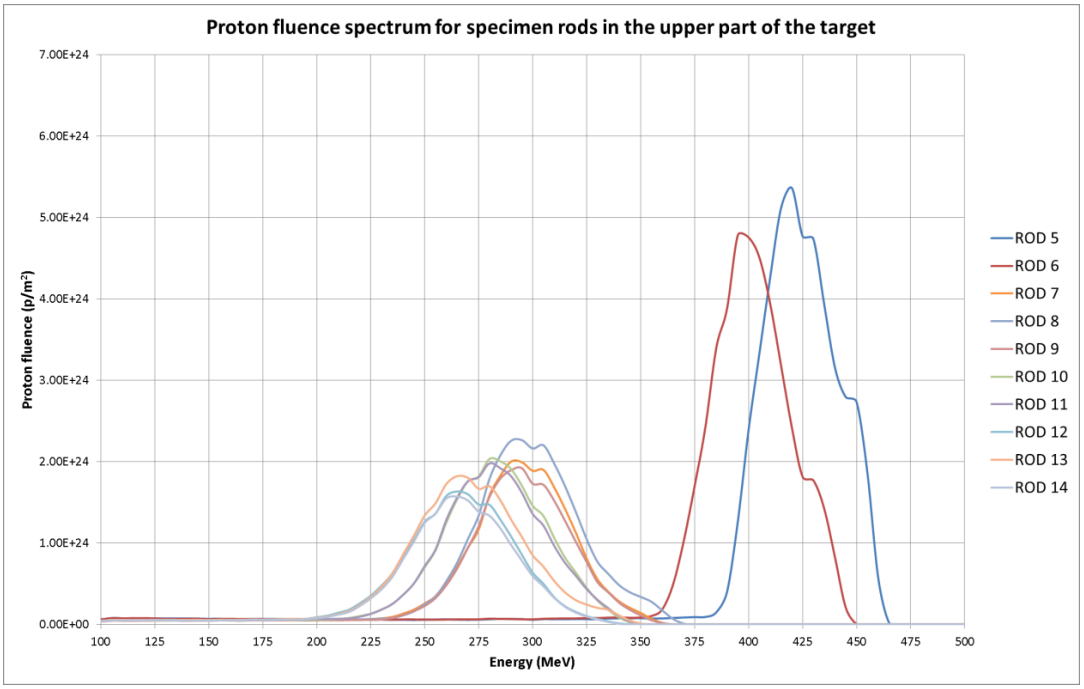

Figure 3.13 Proton fluence spectrum for specimen rods (upper target)

ETSEIB

3.4 NEUTRON FLUENCE IN THE RODS

The neutron fluence over the central rods is presented in *Figure 3.14* and *Figure 3.15*. In the first figure, the neutron fluence is increasing from Row 0 to Row 8, where the maximum is reached, being almost 2.00×10^{26} n/m^2. In the second figure, the neutron fluence is decreasing progressively from Row 10 to Row 36. The curves become flatter with further rows due to the better axially distribution of neutrons. Again, the neutron fluence peak is shifted to the right side due to the proton beam deviation.

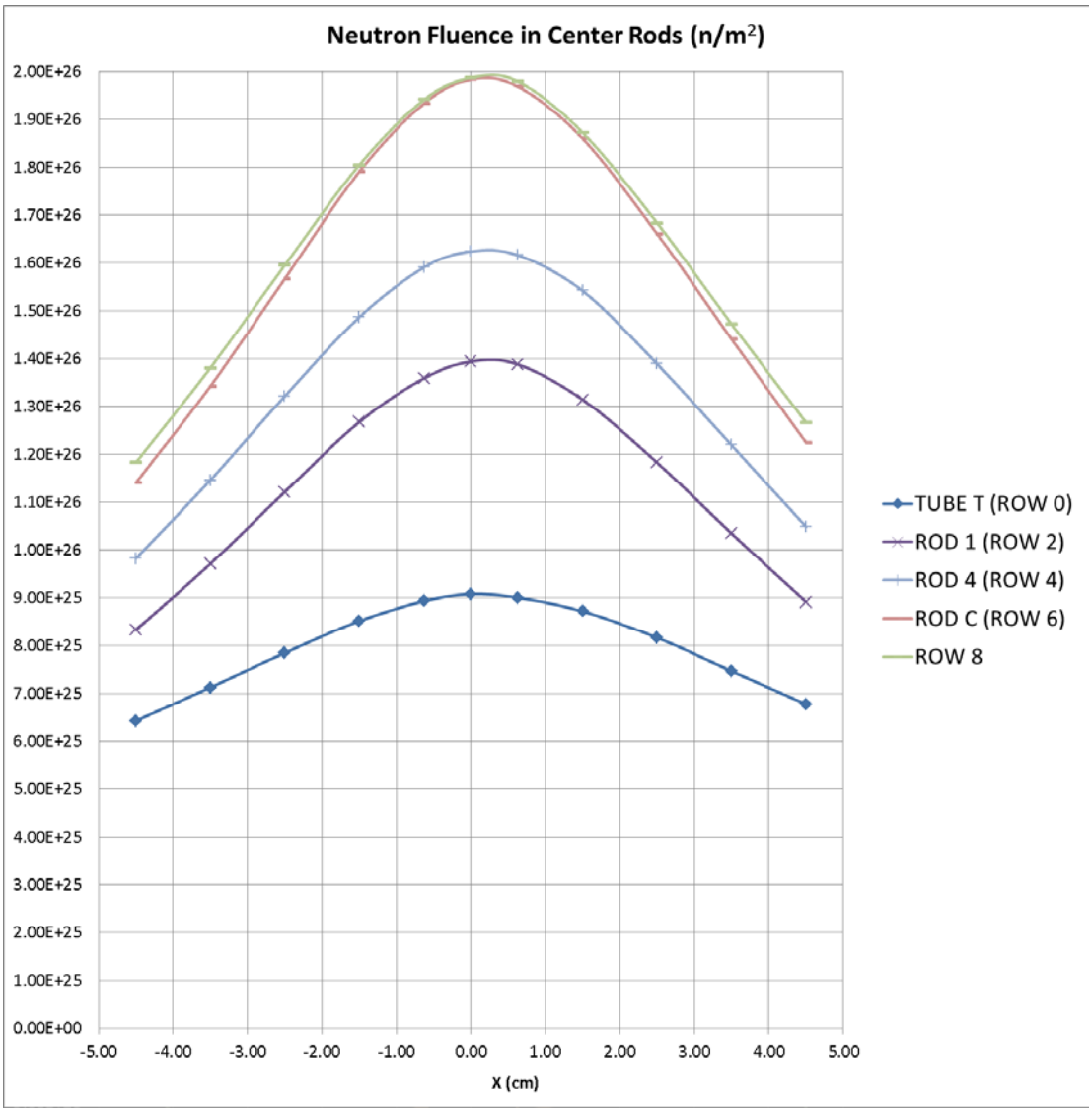

Figure 3.14 Neutron fluence in the center rods (1)

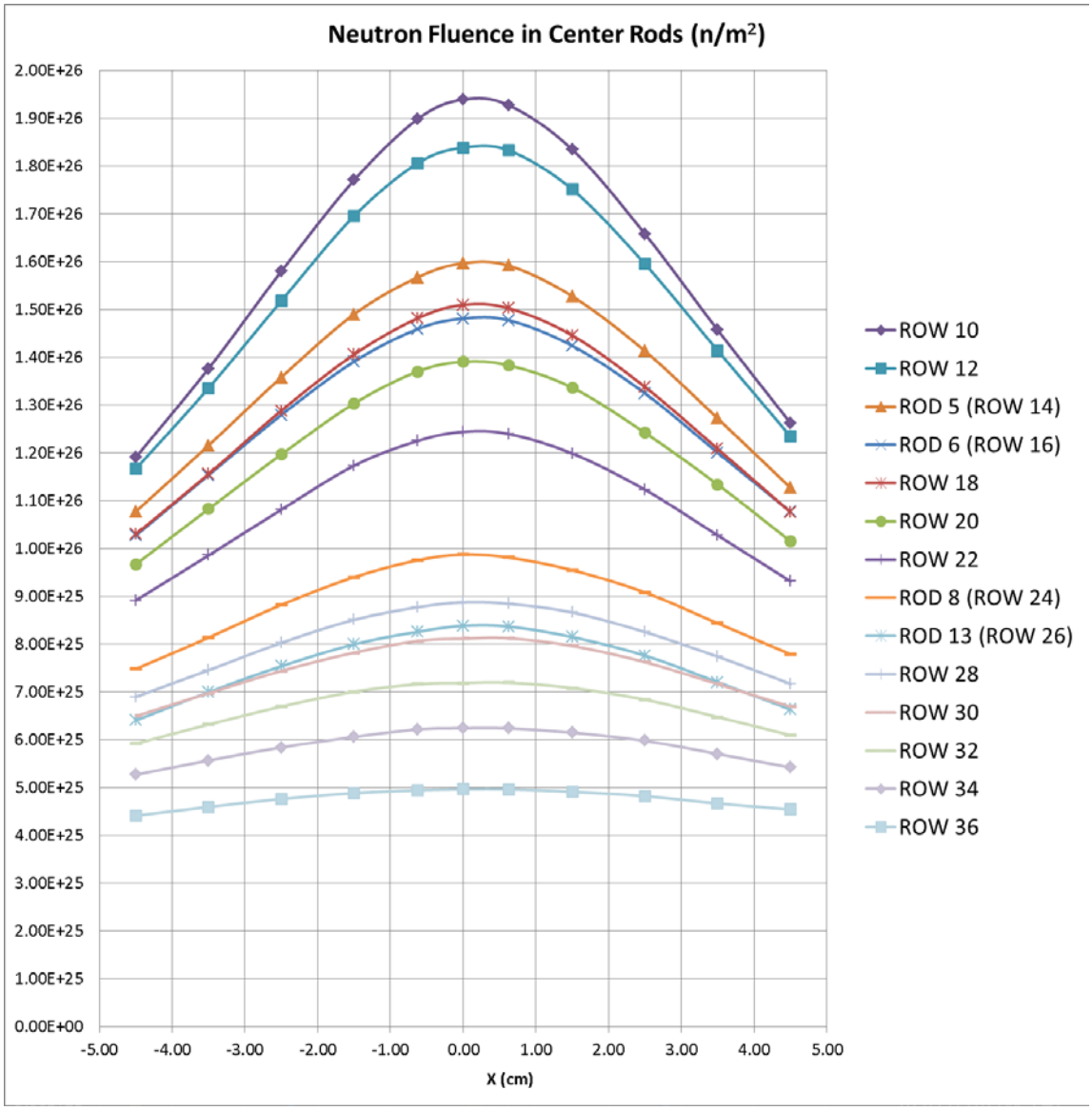

Figure 3.15 Neutron fluence in the center rods (2)

The neutron fluence in the specimen rods placed in the lower and upper part of the target is presented in *Figure 3.16* and *Figure 3.17*, respectively. A similar behavior than for protons is observed here, but taking into account that the neutron fluence is increasing from Row 0 to Row 8. As well as for protons, the left side rods have a higher fluence than right side rods at the center. However, the neutron fluence differences between rods placed in the same row are smaller than those obtained for the proton fluence.

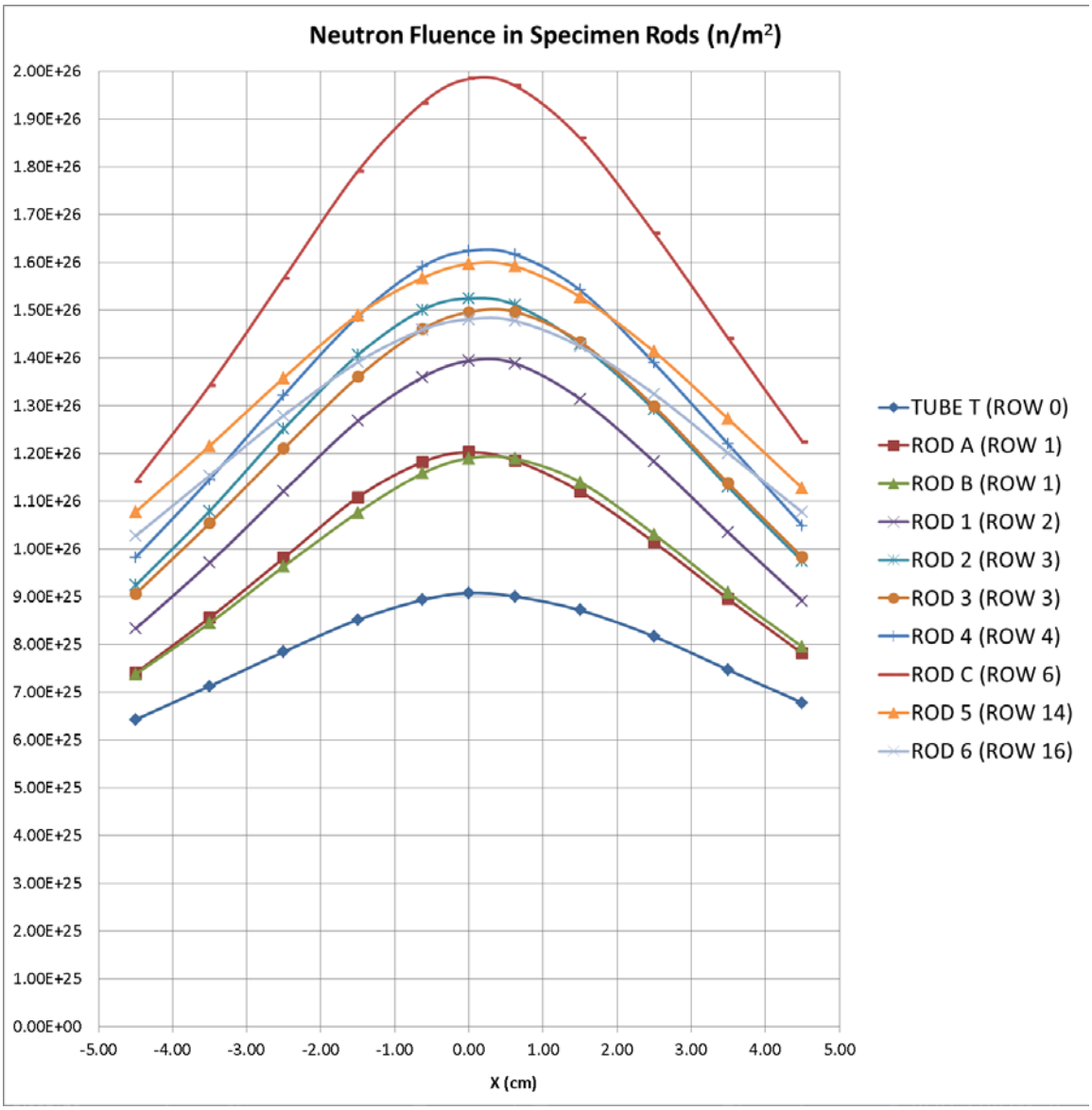

Figure 3.16 Neutron fluence in the specimen rods (lower target)

In the upper part of the target, it is interesting to analyze the rods placed in Row 24 and Row 26. In Row 24, Rod 7 and Rod 8 have a quite similar neutron fluence which is higher than Rod 9. As it has been seen before, the center rod (Rod 8) is expected to have a higher fluence than the left and right side rods. However, this behavior is not seen in *Figure 3.17*. This fact is explained by the material filling the rods which could increase or reduce the neutron fluence up to 10% depending on its composition. This phenomenon is also occurring in Row 26 where the center rod, Rod 13, has a lower neutron fluence than its closest rods placed in the same row.

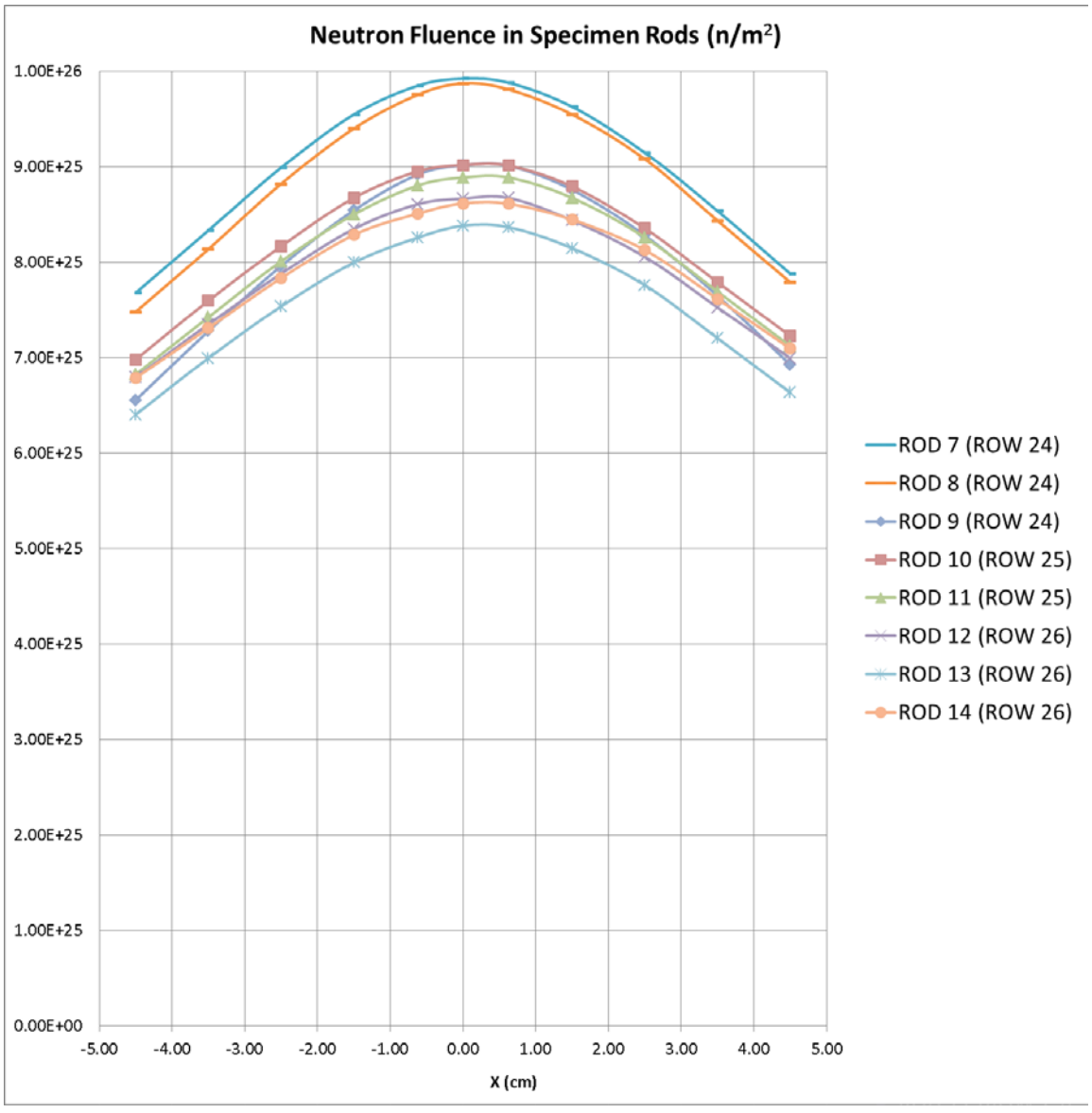

Figure 3.17 Neutron fluence in the specimen rods (upper target)

Finally, the neutron energy spectrum at the center of the specimen rods placed in the lower and upper part of the target is presented in *Figure 3.18* and *Figure 3.19*. The neutron fluence peaks are obtained for really low energies in comparison with the proton energy spectrum. This fact is explained by the spallation interactions, which are generating low-energy neutrons of less than 20 MeV.

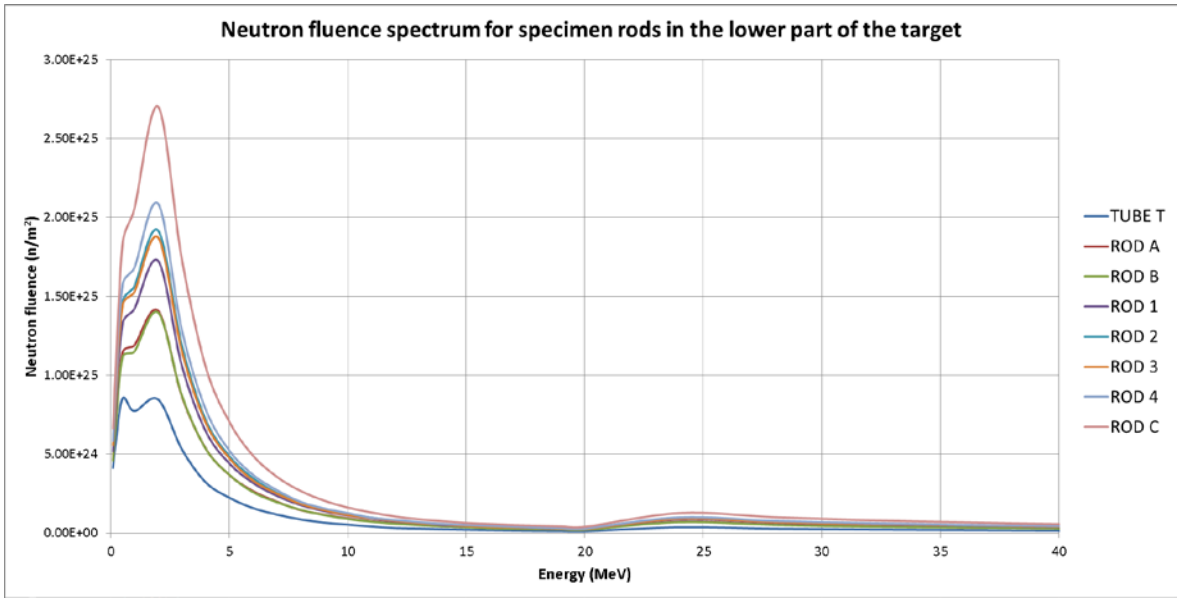

Figure 3.18 Neutron fluence spectrum for specimen rods (lower target)

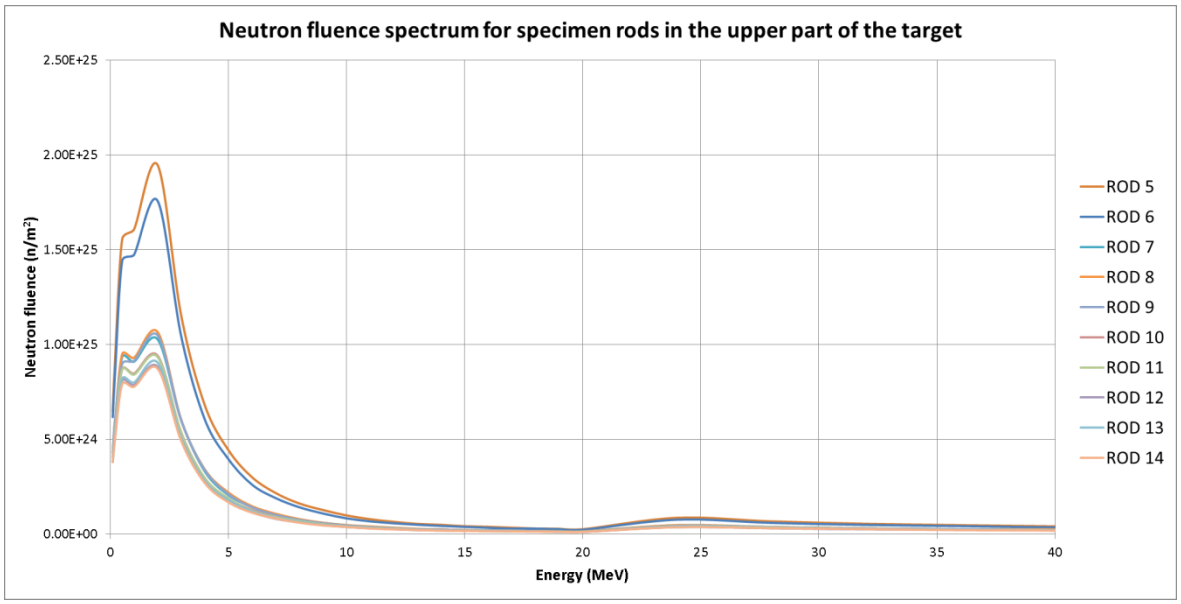

Figure 3.19 Neutron fluence spectrum for specimen rods (upper target)

3.5 MAXIMUM PROTON AND NEUTRON FLUX IN THE RODS

The proton and neutron flux over the central rods have been plotted in *Figure 3.20*. The proton flux is decreasing progressively along the further rows as well as the proton fluence does. Firstly, the neutron flux is increasing from Row 0 to Row 6-8 and then, it is decreasing till Row 36. The behavior of the fast neutrons has been also plotted. The maximum fast neutron flux is 3.25×10^{14} n/(cm^2·s·mA), approximately.

As it has been introduced before, the material filling a rod could affect up to 10% the neutron flux. This phenomenon is happening for Rod 5, Rod 6, Rod 8 and Rod 13 where the material composition is affecting the neutron flux by reducing it around 10%.

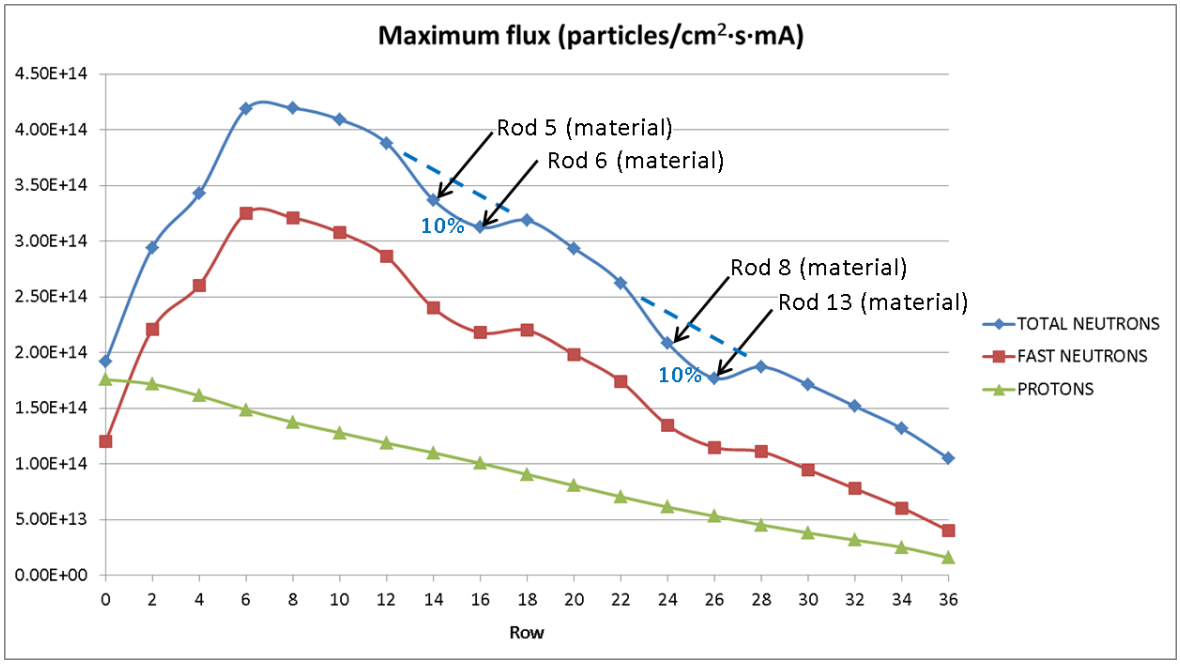

Figure 3.20 Maximum proton and neutron flux in the rods

3.6 PROTON AND NEUTRON FLUENCE IN THE SAFETY HULL

The proton and neutron fluence arriving to the SHT is presented in *Figure 3.21*. The maximum proton fluence is obtained just above Row 36. The proton fluence at this point of the target is very low in comparison with the proton fluence values obtained at the first rows of the target. However, the fact is that the protons have a high probability to interact with the lead target rods which results in more difficulties for reaching the SHT. It makes the proton fluence escape to the SHT at the top of the target where there are no more lead target rods.

Regarding the neutron fluence, the maximum values are obtained in Row 12-13, approximately. As the maximum neutron fluence is obtained in Row 6-8, the maximum neutron fluence in the SHT is expected to be just above of this zone because there, the neutron fluence is high and the probability of interaction for neutrons is really low, in comparison with protons, which allows the possibility of escaping to the SHT.

ROW (approx.)	POSITION	PROTON		NEUTRON	
		OUTER	INNER	OUTER	INNER
	31.725	1.96E+23	2.09E+23	3.10E+25	3.15E+25
	29.325	2.23E+23	2.84E+23	3.42E+25	3.49E+25
Row 35	26.225	2.03E+23	2.75E+23	3.87E+25	3.98E+25
Row 32	23.125	1.91E+23	2.45E+23	4.33E+25	4.47E+25
Row 28-29	19.875	1.93E+23	2.41E+23	4.79E+25	4.97E+25
Row 25	16.625	1.99E+23	2.44E+23	5.22E+25	5.44E+25
Row 22	13.375	2.01E+23	2.47E+23	5.62E+25	5.89E+25
Row 19	10.125	1.92E+23	2.40E+23	5.95E+25	6.26E+25
Row 16	6.875	1.75E+23	2.18E+23	6.16E+25	6.51E+25
Row 12-13	3.625	1.49E+23	1.89E+23	6.21E+25	6.59E+25
Row 9	0.375	1.14E+23	1.49E+23	6.05E+25	6.44E+25
Row 6	-2.875	7.73E+22	1.03E+23	5.64E+25	6.00E+25
Row 3	-6.125	4.30E+22	5.94E+22	4.97E+25	5.26E+25
Row 0	-9.375	1.52E+22	2.17E+22	4.13E+25	4.31E+25

Figure 3.21 Proton and neutron fluence in the Safety Hull (particles/m^2)

Finally, the neutron and proton flux at the SHT is presented in *Figure 3.22* for showing the results in flux units. The water layer between the inner and outer walls of the SHT is reducing a bit the flux.

ROW (approx.)	POSITION	PROTON		NEUTRON	
		OUTER	INNER	OUTER	INNER
	31.725	4.13E+11	4.42E+11	6.54E+13	6.65E+13
	29.325	4.70E+11	5.99E+11	7.22E+13	7.37E+13
Row 35	26.225	4.29E+11	5.80E+11	8.17E+13	8.40E+13
Row 32	23.125	4.04E+11	5.18E+11	9.13E+13	9.43E+13
Row 28-29	19.875	4.08E+11	5.09E+11	1.01E+14	1.05E+14
Row 25	16.625	4.20E+11	5.14E+11	1.10E+14	1.15E+14
Row 22	13.375	4.24E+11	5.22E+11	1.19E+14	1.24E+14
Row 19	10.125	4.04E+11	5.07E+11	1.26E+14	1.32E+14
Row 16	6.875	3.69E+11	4.61E+11	1.30E+14	1.37E+14
Row 12-13	3.625	3.14E+11	4.00E+11	1.31E+14	1.39E+14
Row 9	0.375	2.41E+11	3.14E+11	1.28E+14	1.36E+14
Row 6	-2.875	1.63E+11	2.17E+11	1.19E+14	1.27E+14
Row 3	-6.125	9.08E+10	1.25E+11	1.05E+14	1.11E+14
Row 0	-9.375	3.21E+10	4.58E+10	8.71E+13	9.09E+13

Figure 3.22 Proton and neutron flux in the Safety Hull (particles/cm^2·s·mA)

3.7 ENERGY DEPOSITION IN THE RODS

The energy deposition in the cladding of the rods has been obtained through the MCNPX simulation. The results are expressed in units of MeV/g. These values have been multiplied by the density (g/cm^3) and a factor of 1000 (MeV · mA = kW) in order to obtain the final units of W/(cm^3·mA). The results have been requested in the cladding of the rods to avoid the differences caused by the different material densities filling the rods. However, the cladding of Rod 6, Rod 10, Rod 11 and Rod 12 is made of steel, which has a density of 7.85 g/cm^3, instead of zircaloy, 6.56 g/cm^3.

The results of the maximum energy deposition along the center rods in even rows are plotted in *Figure 3.23*. Firstly, the energy deposition is increasing from Row 0 to Row 2 because Row 0 is just formed by water filling zircaloy tubes. After that, the energy deposition is decreasing progressively till Row 36 with the exception of Row 16 (Rod 6). The cladding of Rod 6 is made of steel and this fact is causing an increase of around 38% in the energy deposition. It is something that was expected because the contribution to the energy deposition for steel cladding rods is up to 35-40%. This phenomenon is not seen for the other steel cladding rods because they are not placed in the center.

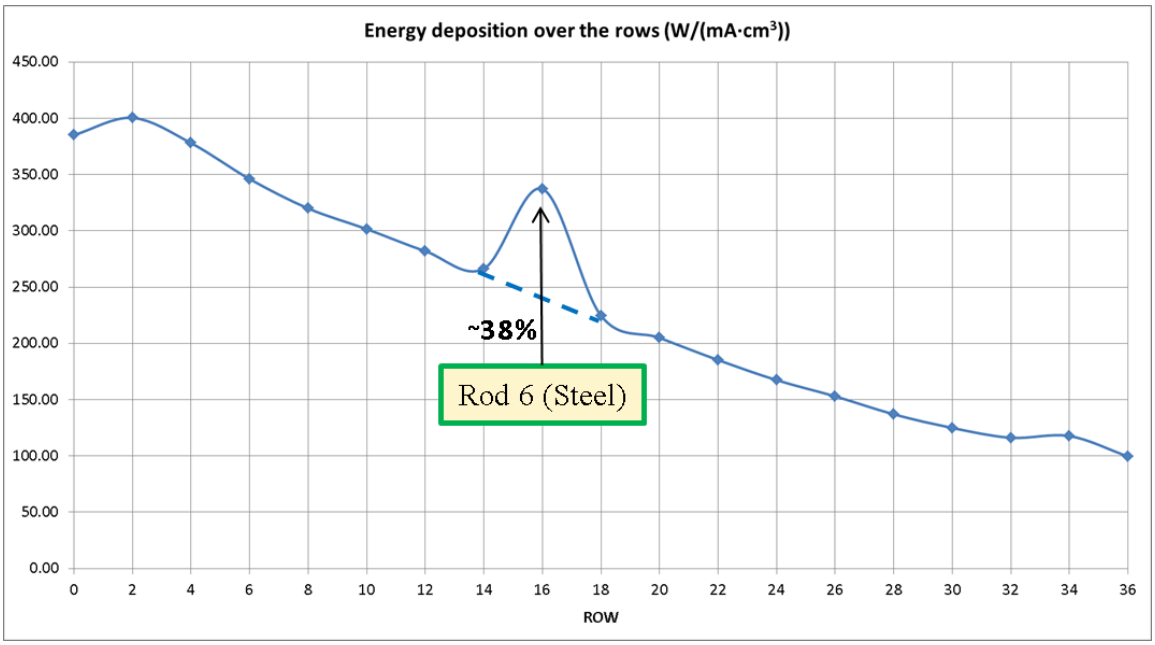

Figure 3.23 Maximum energy deposition in the center rods (W/cm^3·mA)

The energy deposition along the center rods is presented in *Figure 3.24*. It has the same behavior as for the maximum energy deposition. First, there is an increase between Tube T (Row 0) and Rod 1 (Row 2) because Tube T is just water filling zircaloy tubes. Next, the energy deposition is decreasing progressively till Row 36 with the exception of Rod 6, placed in Row 16, due to its cladding which is made of steel. Again, the peak is displaced to the right side due to the proton beam deviation.

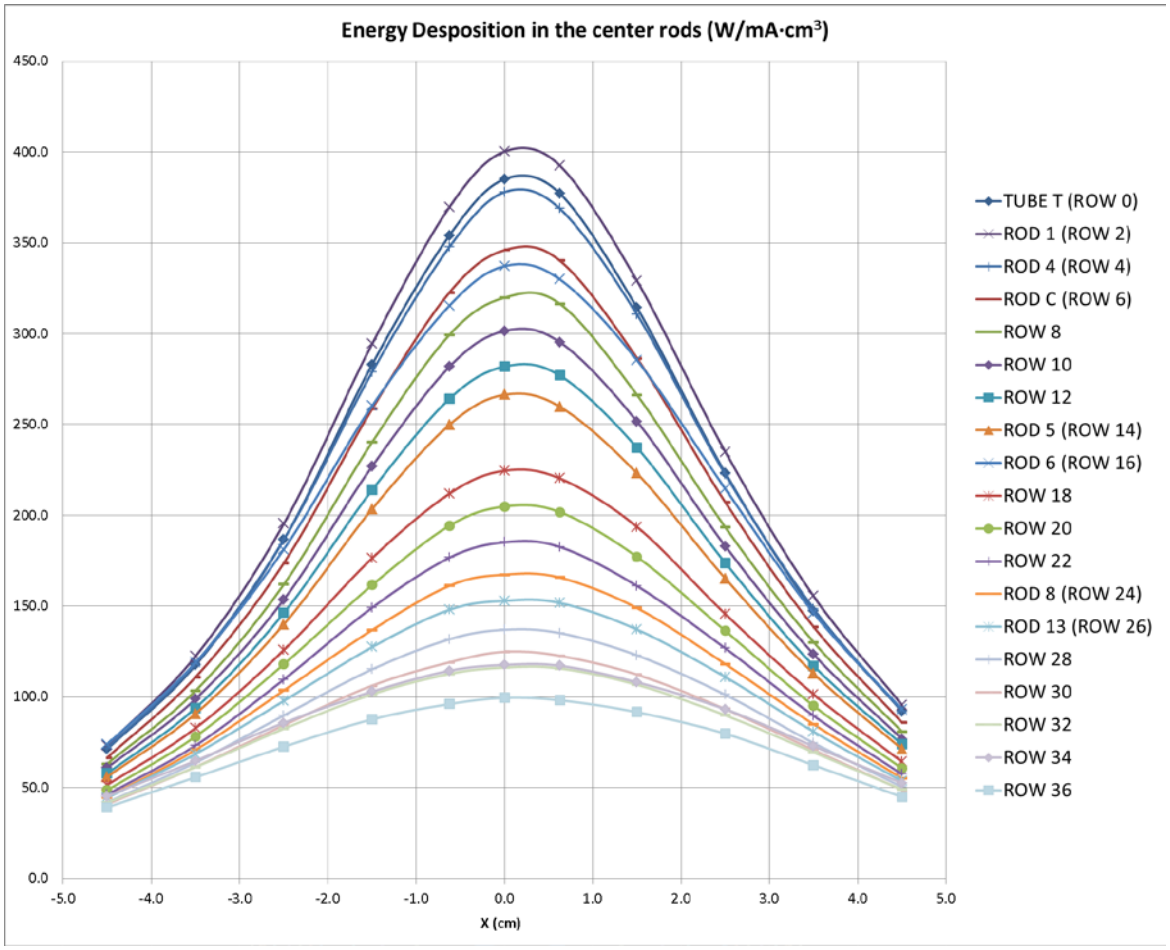

Figure 3.24 Energy deposition in the center rods (W/cm^3·mA)

Regarding the energy deposition in the specimen rods, a similar behavior than the proton fluence is observed again but obtaining higher values for steel cladding rods. *Figure 3.25* is showing the energy deposition in the specimen rods interspersed along the Target.

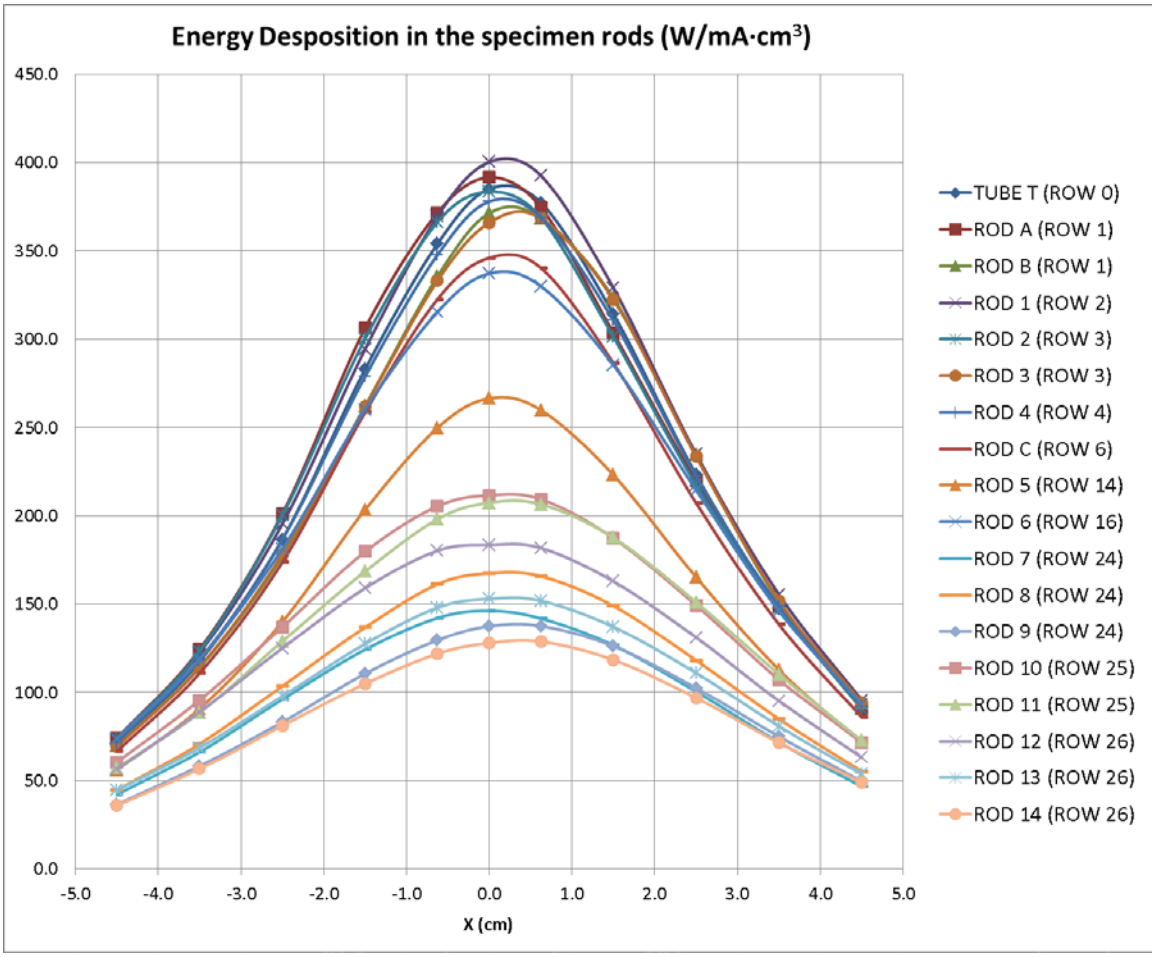

Figure 3.25 Energy deposition in the specimen rods (W/cm^3·mA)

4. STIP VI – TARGET 9. RADIATION DAMAGE CALCULATIONS

The displacement per atom plus the Helium and Hydrogen concentration have been calculated as the irradiation parameters for estimating the radiation damage. These calculations have been performed multiplying the neutron and proton fluences by the corresponding cross section at each energy range. The cross section data [10] used for those calculations have been obtained from United States and it has been also applied at PSI through the previous STIP experiments. The expression used for these calculations and its factor components are described next.

$$R = \sum \Phi(E) \cdot X\,(E) \qquad (2)$$

R Radiation Damage. The unit is displacement per atom (dpa) or product concentration in atomic parts per million (appm)

$\Phi(E)$ Neutron and Proton fluence at each energy range. The unit is neutrons or protons divided by square meters (n/m^2 or p/m^2).

$\mathrm{X}\,(E)$ Cross section at each energy range. Different cross sections are used depending on the particle and the radiation product which is being calculated. The units are expressed in barns (10^{-28} m^2).

The final results of the irradiation parameters for the specimen rods, the calotte and the SHT are commented in the following lines.

4.1 RADIATION DAMAGE IN THE CALOTTE

The radiation damage in the calotte is calculated using the Aluminum cross section data. The maximum values obtained for each irradiation parameter are 8.85 dpa, 2447.36 appm He and 4853.74 appm H. The results are presented in *Figure 4.1*, *Figure 4.2* and *Figure 4.3*.

Y \ X (cm)	-1.50	-0.75	-0.25	0.25	0.75	1.50
1.75	6.04	6.63	6.75	6.92	6.64	6.01
1.25	6.88	7.38	7.68	7.85	7.62	6.79
0.75	7.53	8.13	8.42	8.47	8.34	7.54
0.25	7.69	8.54	8.83	8.85	8.74	7.67
-0.25	7.43	8.19	8.59	8.48	8.45	7.61
-0.75	6.97	7.81	8.11	8.10	7.98	7.22
-1.25	6.11	6.58	6.84	7.07	6.79	6.14
-1.75	5.26	5.68	5.99	6.06	5.79	5.35

Figure 4.1 Total displacement per atom (dpa)

Y \ X (cm)	-1.50	-0.75	-0.25	0.25	0.75	1.50
1.75	1487.96	1664.48	1705.93	1756.36	1678.46	1481.30
1.25	1769.04	1929.91	2034.65	2064.12	2009.02	1733.34
0.75	1992.24	2213.68	2308.45	2318.14	2246.40	1982.25
0.25	2045.65	2341.24	2447.36	2447.18	2391.61	2032.51
-0.25	1958.69	2217.88	2354.90	2322.72	2298.60	2030.56
-0.75	1785.89	2075.96	2173.04	2176.44	2119.13	1893.98
-1.25	1486.21	1647.43	1744.19	1797.83	1729.11	1513.01
-1.75	1209.63	1337.69	1446.40	1457.48	1382.97	1242.66

Figure 4.2 Total Helium concentration (appm He)

Y \ X (cm)	-1.50	-0.75	-0.25	0.25	0.75	1.50
1.75	2956.31	3306.19	3387.85	3486.94	3334.37	2943.18
1.25	3513.44	3833.66	4040.62	4097.44	3988.76	3443.72
0.75	3955.80	4391.12	4581.54	4598.65	4460.06	3935.52
0.25	4059.73	4642.93	4851.89	4853.74	4745.83	4034.22
-0.25	3888.40	4399.75	4667.40	4607.05	4558.71	4028.81
-0.75	3546.70	4120.89	4312.14	4319.08	4204.59	3759.34
-1.25	2954.26	3273.49	3464.39	3571.21	3431.70	3005.34
-1.75	2403.81	2659.85	2875.60	2896.92	2748.24	2472.04

Figure 4.3 Total Hydrogen concentration (appm H)

The contribution of neutrons for each irradiation parameter calculated is also presented in the following figures. As it can be observed, the neutron contribution for the Helium and Hydrogen production is almost negligible. This fact is due to the cross section data which is much higher for high energy protons than for low energy neutrons because the fluence of neutrons and protons in the calotte is about the same order of magnitude.

Y \ X (cm)	-1.50	-0.75	-0.25	0.25	0.75	1.50
1.75	37.33%	36.02%	35.63%	35.34%	35.73%	37.33%
1.25	34.55%	32.96%	32.49%	32.89%	33.00%	34.99%
0.75	32.59%	30.91%	30.34%	30.44%	31.32%	32.96%
0.25	32.20%	30.42%	29.60%	29.62%	30.42%	32.58%
-0.25	32.84%	31.09%	30.57%	30.46%	30.75%	32.19%
-0.75	34.74%	32.49%	31.73%	31.68%	32.37%	33.42%
-1.25	37.95%	36.14%	35.08%	35.17%	35.62%	37.33%
-1.75	41.60%	39.95%	38.53%	38.58%	39.47%	40.80%

Figure 4.4 Neutron contribution to displacement per atom (%)

Y \ X (cm)	-1.50	-0.75	-0.25	0.25	0.75	1.50
1.75	0.86%	0.84%	0.84%	0.81%	0.83%	0.85%
1.25	0.81%	0.77%	0.73%	0.78%	0.75%	0.82%
0.75	0.74%	0.71%	0.70%	0.69%	0.71%	0.75%
0.25	0.75%	0.69%	0.68%	0.68%	0.67%	0.74%
-0.25	0.75%	0.69%	0.70%	0.69%	0.70%	0.73%
-0.75	0.80%	0.77%	0.71%	0.73%	0.76%	0.76%
-1.25	0. 89%	0.84%	0.79%	0.83%	0.81%	0.87%
-1.75	1.01%	0.98%	0.91%	0.92%	0.93%	0.96%

Figure 4.5 Neutron contribution to Helium concentration (%)

Y \ X (cm)	-1.50	-0.75	-0.25	0.25	0.75	1.50
1.75	1.48%	1.47%	1.42%	1.39%	1.42%	1.46%
1.25	1.39%	1.34%	1.31%	1.34%	1.32%	1.42%
0.75	1.30%	1.23%	1.24%	1.21%	1.27%	1.29%
0.25	1.27%	1.19%	1.19%	1.18%	1.20%	1.28%
-0.25	1.30%	1.20%	1.19%	1.22%	1.22%	1.24%
-0.75	1.39%	1.32%	1.23%	1.25%	1.29%	1.32%
-1.25	1.54%	1.46%	1.39%	1.39%	1.39%	1.48%
-1.75	1.68%	1.63%	1.55%	1.56%	1.57%	1.69%

Figure 4.6 Neutron contribution to Hydrogen concentration (%)

4.2 RADIATION DAMAGE IN THE SAFETY HULL TUBE

The irradiation parameters calculated in the SHT for Aluminum are presented from *Figure 4.7* to *Figure 4.9*. The maximum values are obtained around the middle part of the target. The maximum displacement per atom is obtained around Row 12-13 with a value of 3.14 dpa. The maximum Helium and Hydrogen concentration are obtained around Row 16 with the following values: 17.63 appm He and 71.64 appm H.

The contribution of protons is increasing from the lower part to the upper part of the SHT, as well as the proton fluence does, because less proton fluence is escaping from the lower part of the target. The fact is that the proton fluence arriving to the lower part of the SHT is really low in comparison with the neutron fluence due to their high probability of interaction. Actually, the proton fluence is around 2-3 orders of magnitude lower than the neutron fluence in the SHT. The contribution of protons to the displacement per atom is quite low in comparison with the contribution to the Helium and Hydrogen production because of the Aluminum cross section data.

ROW (approx.)	POSITION	NEUTRONS		PROTONS		TOTAL (dpa)	
		OUTER	INNER	OUTER	INNER	OUTER	INNER
	31.725	91.92%	91.67%	8.08%	8.33%	0.58	0.63
	29.325	93.69%	92.44%	6.31%	7.56%	0.76	0.85
Row 35	26.225	96.10%	95.34%	3.90%	4.66%	1.02	1.15
Row 32	23.125	97.10%	96.79%	2.90%	3.21%	1.29	1.45
Row 28-29	19.875	97.62%	97.42%	2.38%	2.58%	1.58	1.78
Row 25	16.625	97.94%	97.82%	2.06%	2.18%	1.87	2.11
Row 22	13.375	98.20%	98.09%	1.80%	1.91%	2.16	2.44
Row 19	10.125	98.44%	98.34%	1.56%	1.66%	2.42	2.75
Row 16	6.875	98.67%	98.58%	1.33%	1.42%	2.62	2.99
Row 12-13	3.625	98.88%	98.79%	1.12%	1.21%	2.74	3.14
Row 9	0.375	99.09%	99.00%	0.91%	1.00%	2.72	3.13
Row 6	-2.875	99.28%	99.20%	0.72%	0.80%	2.50	2.88
Row 3	-6.125	99.47%	99.38%	0.53%	0.62%	2.06	2.37
Row 0	-9.375	99.70%	99.64%	0.30%	0.36%	1.49	1.69

Figure 4.7 Displacement per atom in the Safety Hull

ROW (approx.)	POSITION	NEUTRONS		PROTONS		TOTAL (appm He)	
		OUTER	INNER	OUTER	INNER	OUTER	INNER
	31.725	63.97%	63.45%	36.03%	36.55%	7.49	7.99
	29.325	66.25%	61.50%	33.75%	38.50%	8.67	9.99
Row 35	26.225	73.96%	69.57%	26.04%	30.43%	9.49	10.97
Row 32	23.125	77.55%	75.24%	22.45%	24.76%	10.61	12.04
Row 28-29	19.875	79.33%	77.46%	20.67%	22.54%	11.93	13.53
Row 25	16.625	80.42%	79.13%	19.58%	20.87%	13.21	14.99
Row 22	13.375	81.54%	80.14%	18.46%	19.86%	14.29	16.35
Row 19	10.125	83.06%	81.50%	16.94%	18.50%	15.00	17.31
Row 16	6.875	84.70%	83.38%	15.30%	16.62%	15.21	17.63
Row 12-13	3.625	86.49%	85.24%	13.51%	14.76%	14.78	17.29
Row 9	0.375	88.61%	87.32%	11.39%	12.68%	13.53	15.92
Row 6	-2.875	90.72%	89.52%	9.28%	10.48%	11.33	13.35
Row 3	-6.125	92.89%	91.63%	7.11%	8.37%	8.34	9.79
Row 0	-9.375	95.97%	95.00%	4.03%	5.00%	5.35	6.12

Figure 4.8 Helium concentration in the Safety Hull

ROW (approx.)	POSITION	NEUTRONS		PROTONS		TOTAL (appm H)	
		OUTER	INNER	OUTER	INNER	OUTER	INNER
	31.725	58.66%	58.06%	41.34%	41.94%	34.04	36.34
	29.325	61.26%	56.13%	38.74%	43.87%	38.98	45.44
Row 35	26.225	70.00%	64.98%	30.00%	35.02%	41.37	48.30
Row 32	23.125	74.54%	71.92%	25.46%	28.08%	45.29	51.53
Row 28-29	19.875	76.81%	74.80%	23.19%	25.20%	50.27	57.00
Row 25	16.625	78.28%	76.87%	21.72%	23.13%	55.11	62.42
Row 22	13.375	79.61%	78.30%	20.39%	21.70%	59.15	67.37
Row 19	10.125	81.20%	79.84%	18.80%	20.16%	61.65	70.70
Row 16	6.875	82.85%	81.70%	17.15%	18.30%	62.10	71.64
Row 12-13	3.625	84.63%	83.45%	15.37%	16.55%	59.92	69.71
Row 9	0.375	86.64%	85.38%	13.36%	14.62%	54.13	63.47
Row 6	-2.875	88.65%	87.40%	11.35%	12.60%	44.51	52.42
Row 3	-6.125	90.77%	89.32%	9.23%	10.68%	31.90	37.48
Row 0	-9.375	94.42%	93.13%	5.58%	6.87%	19.57	22.42

Figure 4.9 Hydrogen concentration in the Safety Hull

4.3 RADIATION DAMAGE IN THE SPECIMEN RODS

The irradiation parameters of displacement per atom plus Helium and Hydrogen production have been calculated for all the specimen rods. However, the irradiation parameters are just presented next for Rod 1, Rod 5 and Rod 8 which are placed in the lower, middle and upper part of the target. All the results for the specimen rods are presented in *Annex B. Radiation Damage Calculations*.

As different materials are fitting the specimen rods, the displacement per atom and the Helium production have been calculated for the following materials: martensitic steel containing 9% Chromium and 1% Molybdenum (9Cr-1Mo), Zircaloy-2 (Zry-2), Aluminum (Al), Silicon Carbide (SiC), Tantalum (Ta) and Tungsten (W). The irradiation parameter of Hydrogen production is just calculated for martensitic steel 9Cr-1Mo, Zircaloy-2, Aluminum and Tantalum.

First of all, the maximum proton and neutron fluence in Rod 1, Rod 5 and Rod 8 is presented in *Figure 4.10*.

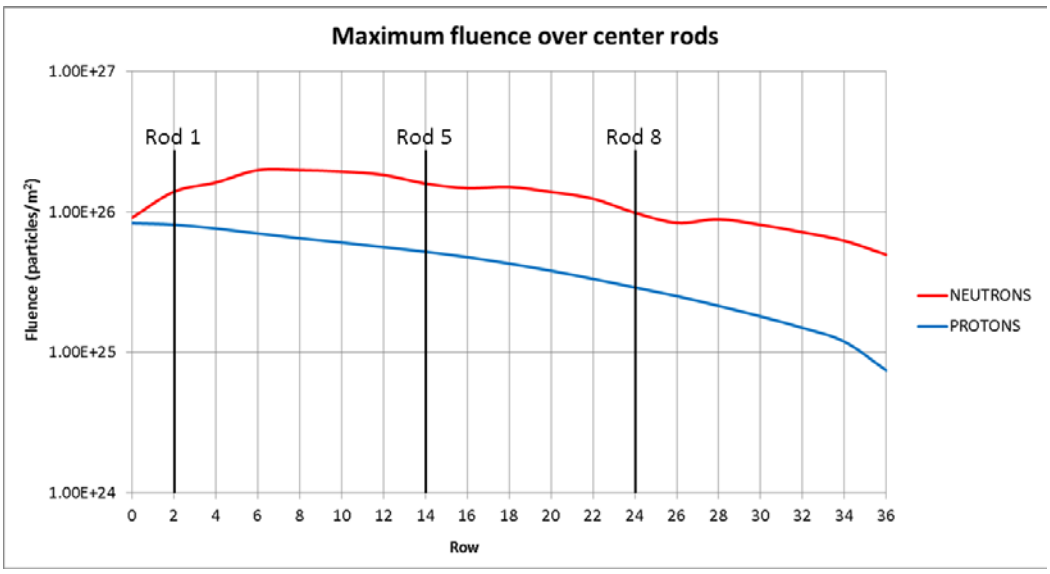

Figure 4.10 Proton and Neutron fluence in Rod 1, Rod 5 and Rod 8

4.3.1 DISPLACEMENT PER ATOM

The maximum displacement per atom in Rod 1, Rod 5 and Rod 8 has been obtained for Zircaloy-2 with values of 72.07 dpa, 48.97 dpa and 25.82 dpa, respectively.

Figure 4.11, *Figure 4.12* and *Figure 4.13* are showing the displacement per atom for each material in Rod 1, Rod 5 and Rod 8.

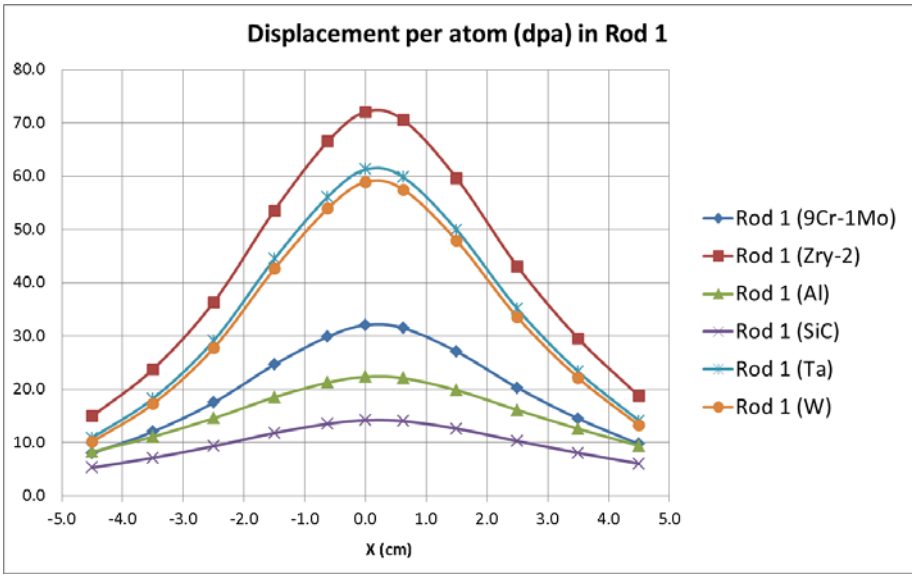

Figure 4.11 Displacement per atom in Rod 1

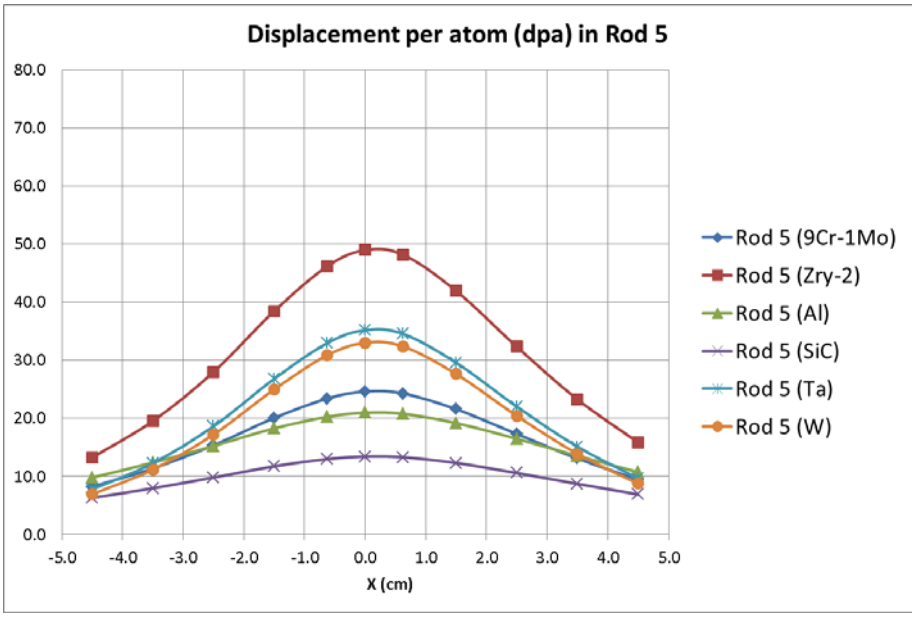

Figure 4.12 Displacement per atom in Rod 5

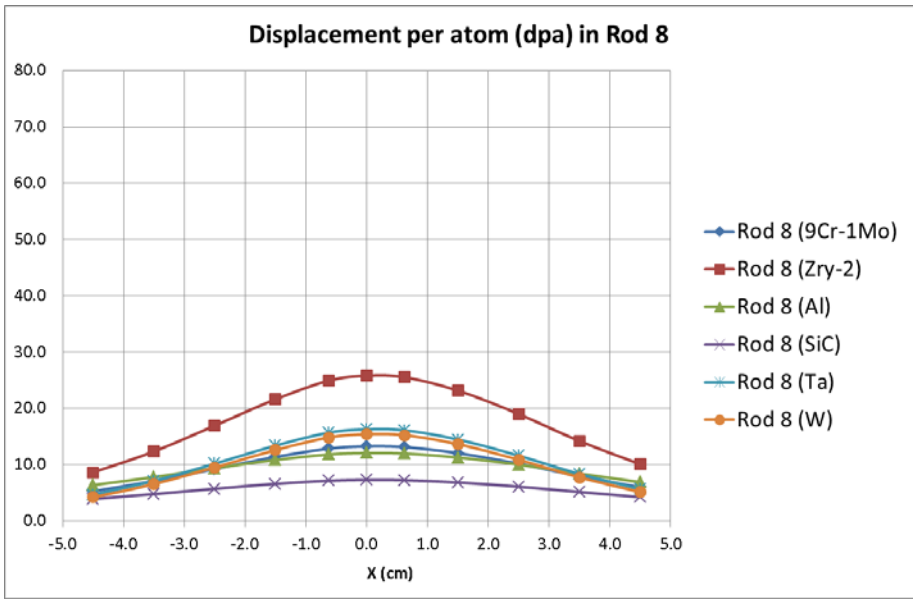

Figure 4.13 Displacement per atom in Rod 8

The differences between the materials are caused by the different cross section, but these cross sections used for calculating the displacement per atom are strongly related with the concepts of *Primary Knock-on Atom* (PKA) and *Threshold Displacement Energy* (E_d).

The PKA is defined as the first atom that is displaced from its lattice site due to the collision with the incident particle coming from irradiation. This displacement can induce subsequent lattice site displacements in other atoms or come to rest in an interstitial site depending on its energy. The E_d is the energy required to overcome the potential barrier to move the atom from one lattice site to another. It depends on the nuclei present and the structure of the material. The minimum kinetic energy is around 2-3 times this threshold value because not all the energy is transferred in the scattering process. The maximum displacement per atom is found in Zircaloy-2 and the minimum in Silicon Carbide.

Finally, *Figure 4.14*, *Figure 4.15* and *Figure 4.16* are showing the neutron and proton contribution to the displacement per atom for Zircaloy-2 in Rod 1, Rod 5 and Rod 8. Protons are the main contributor in all of them. This fact is caused by the bigger values of the cross section data for the high energy protons in comparison with the low energy neutrons.

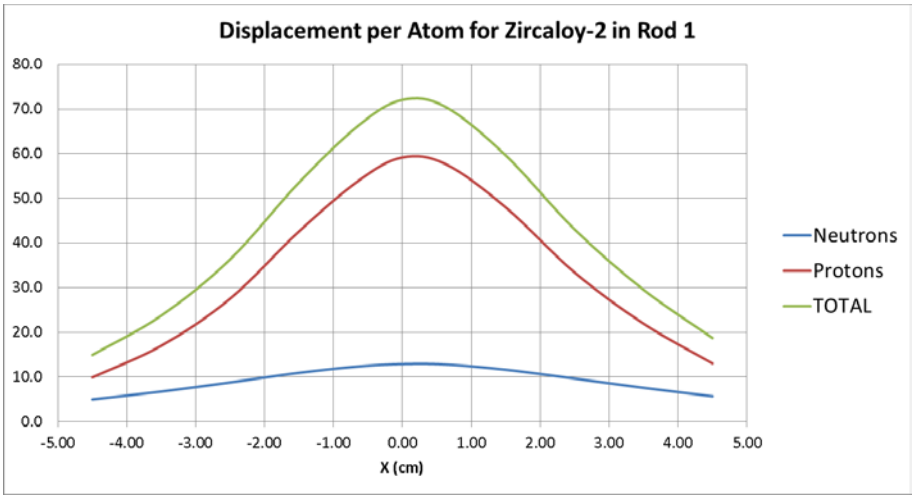

Figure 4.14 Displacement per atom for Zircaloy-2 in Rod 1

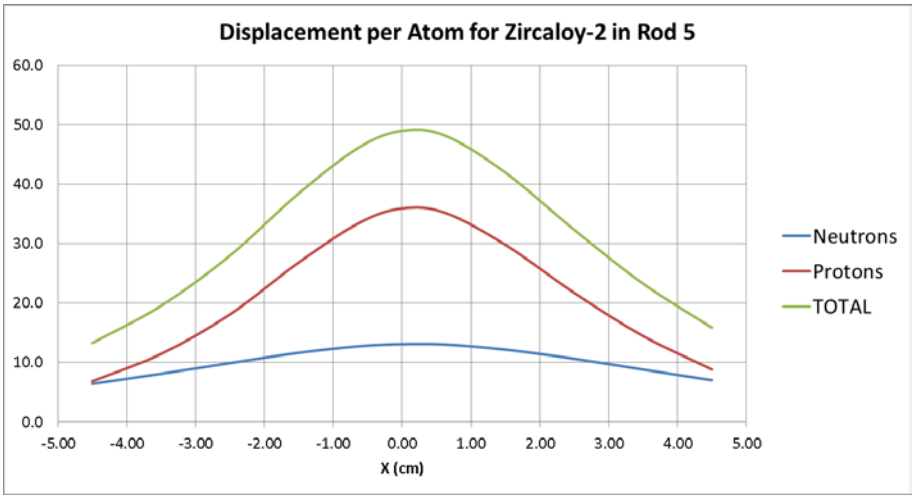

Figure 4.15 Displacement per atom for Zircaloy-2 in Rod 5

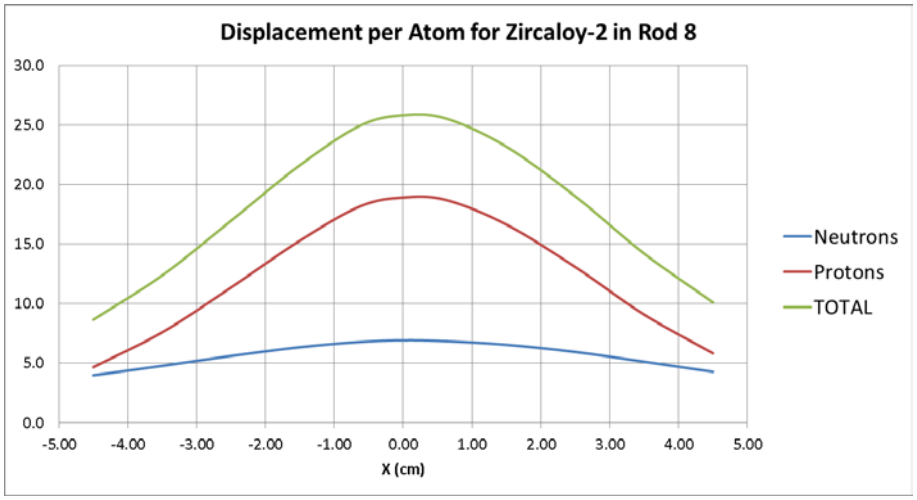

Figure 4.16 Displacement per atom for Zircaloy-2 in Rod 8

4.3.2 HELIUM CONCENTRATION

The Helium production for different materials in Rod 1, Rod 5 and Rod 8 is presented in *Figure 4.17*, *Figure 4.18* and *Figure 4.19*. The maximum Helium concentration is obtained for Tantalum in Rod 1 and for Silicon Carbide in Rod 5 and Rod 8. The maximum values are 3545.26 appm He, 1649.28 appm He and 822.98 appm He, respectively.

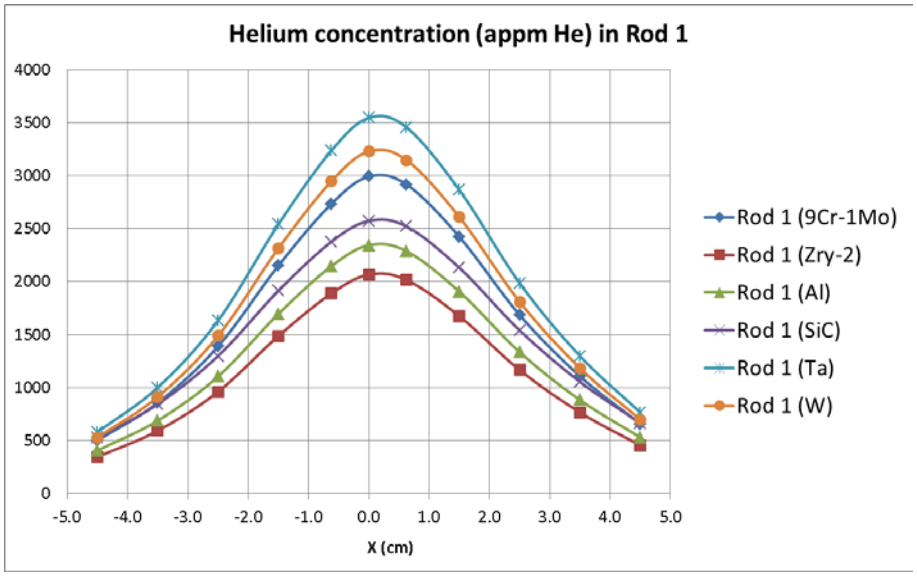

Figure 4.17 Helium concentration in Rod 1

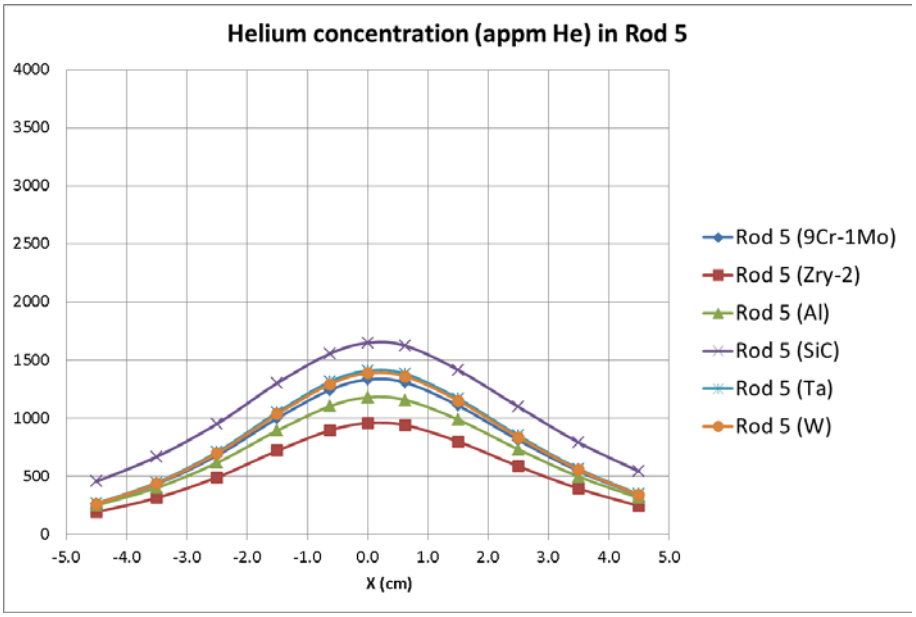

Figure 4.18 Helium concentration in Rod 5

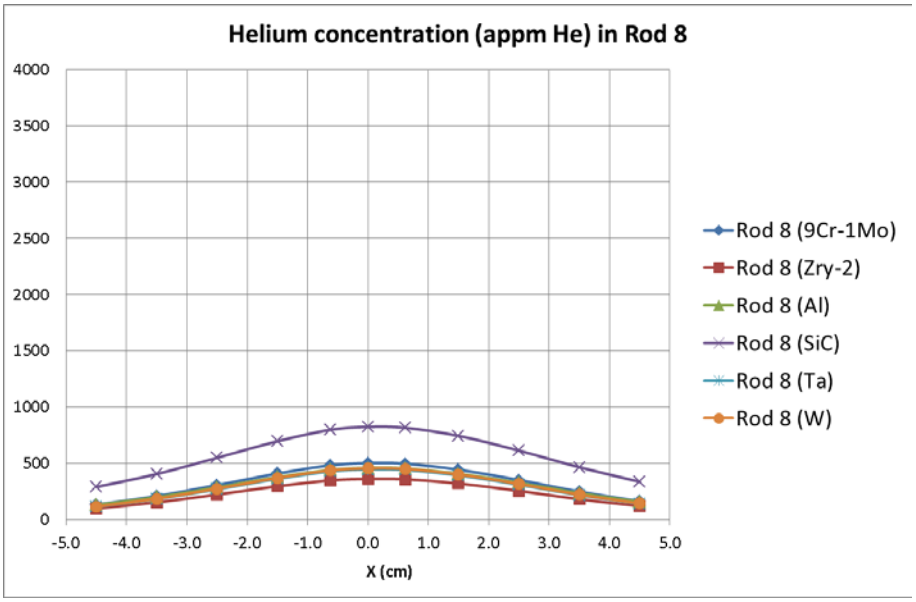

Figure 4.19 Helium concentration in Rod 8

Figure 4.20, Figure 4.21 and *Figure 4.22* are showing the contribution of protons and neutrons for the material which causes the maximum Helium concentration. There is an insignificant contribution of neutrons in Rod 1 for the Helium production in Tantalum. The main contributor in Rod 5 and Rod 8 for the Helium production in Silicon Carbide is protons but, the neutron contribution is significant coming approximately from 50% at the end of the rod to 30% at the center. Again, the differences in Rod 1 (Tantalum) are caused by the bigger values of the cross section data for the high energy protons in comparison with the low energy neutrons. However, the differences in the proton and neutron cross section for the Helium production in Silicon Carbide are quite low as the contribution of neutrons becomes significant.

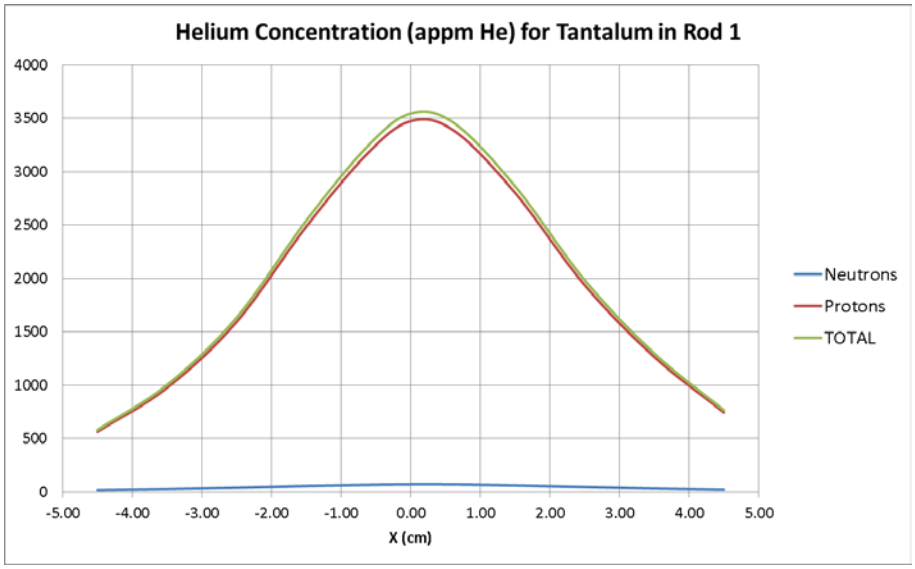

Figure 4.20 Helium concentration for Tantalum in Rod 1

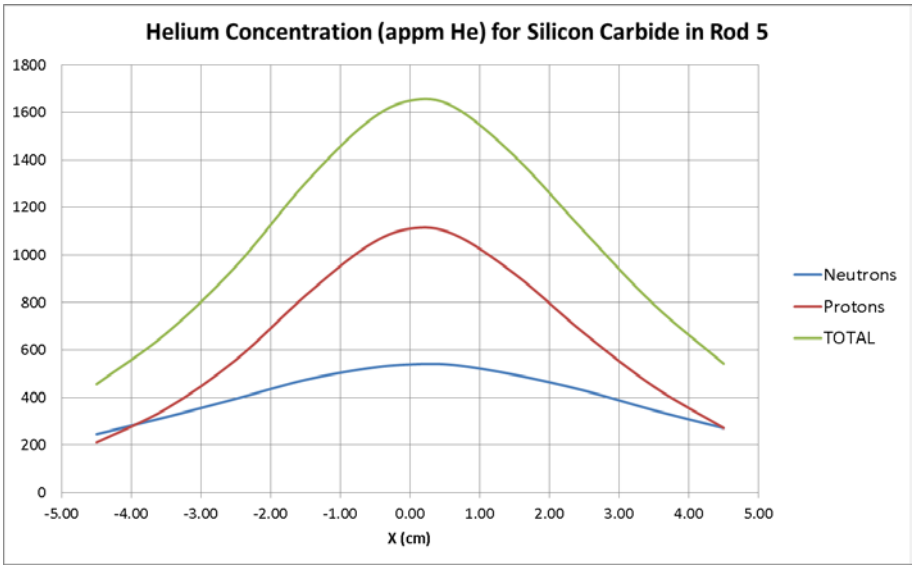

Figure 4.21 Helium concentration for Silicon Carbide in Rod 5

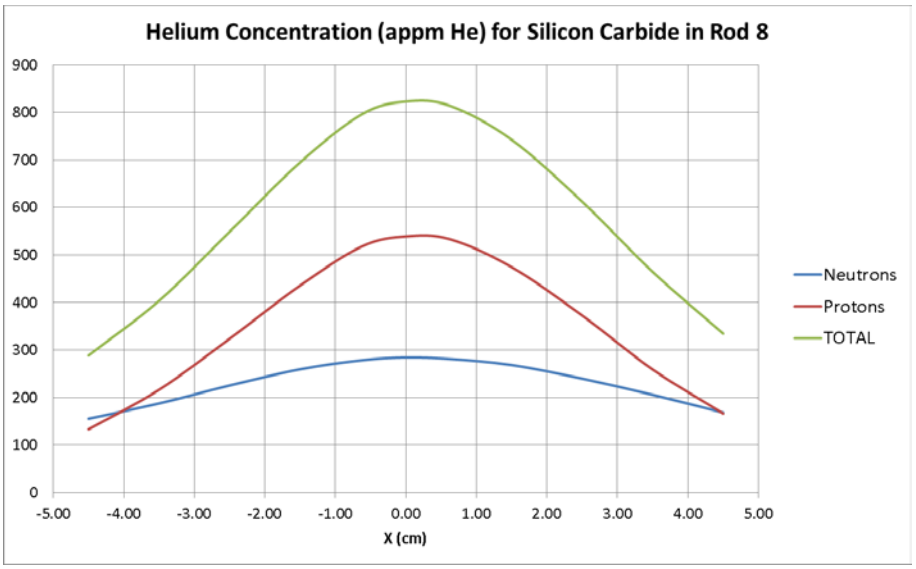

Figure 4.22 Helium concentration for Silicon Carbide in Rod 8

4.3.3 HYDROGEN CONCENTRATION

The Hydrogen production for different materials in Rod 1, Rod 5 and Rod 8 is presented in *Figure 4.23*, *Figure 4.24* and *Figure 4.25*. The maximum Hydrogen concentration is obtained for Tantalum in Rod 1 and Rod 5, and for the martensitic steel 9Cr-1Mo in Rod 8. The maximum values are 17176.72 appm H, 7774.66 appm H and 3247.35 appm H, respectively.

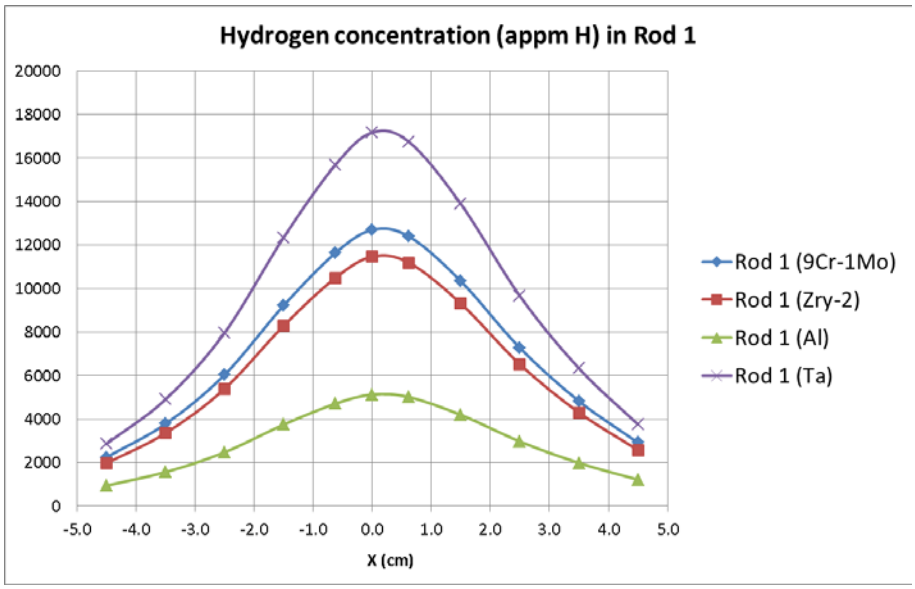

Figure 4.23 Hydrogen concentration in Rod 1

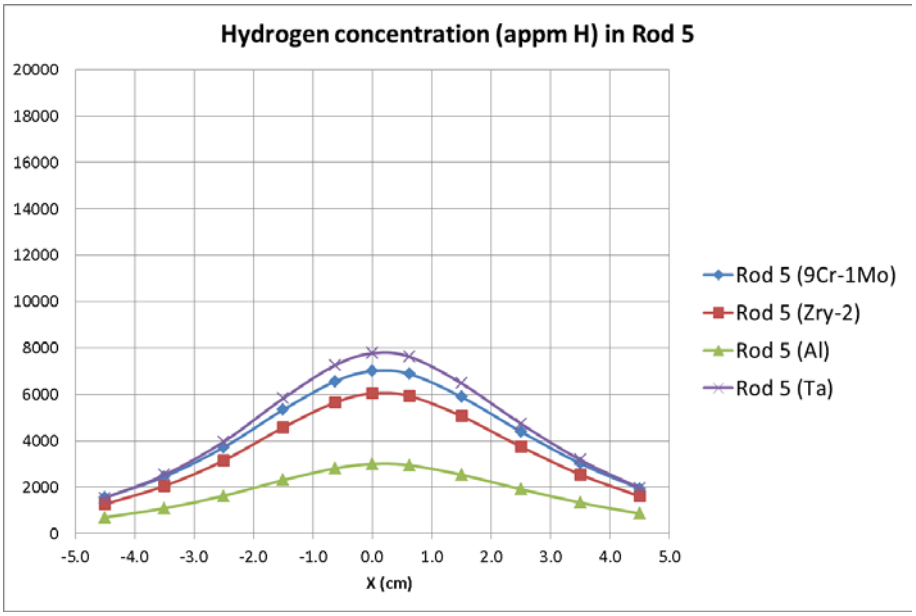

Figure 4.24 Hydrogen concentration in Rod 5

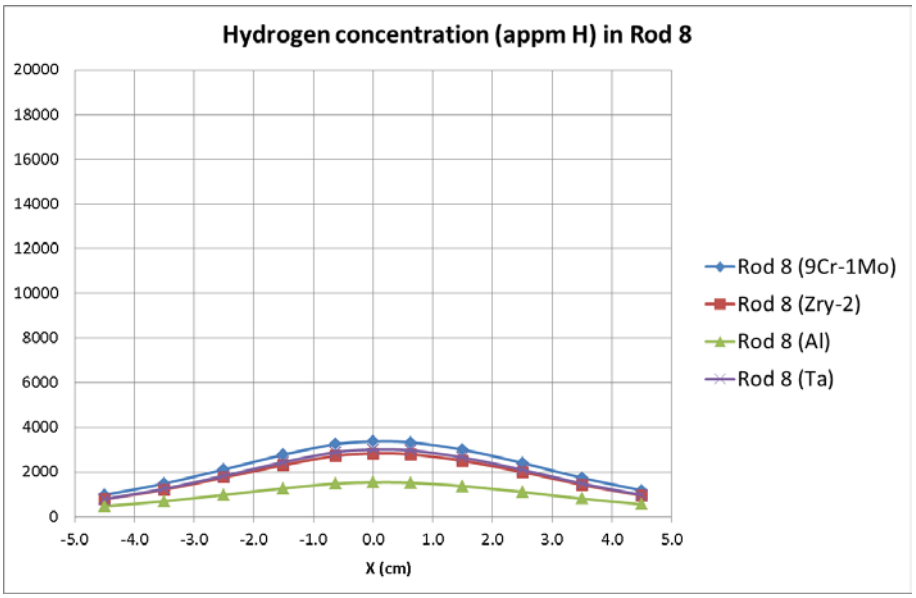

Figure 4.25 Hydrogen concentration in Rod 8

Figure 4.26, *Figure 4.27* and *Figure 4.28* are showing the contribution of protons and neutrons for the material which causes the maximum Hydrogen concentration. The contribution of neutrons is negligible in Rod 1 and quite low in Rod 5 and Rod 8. It happens the same as mentioned before, the values of the Hydrogen production cross section data for the high energy protons are higher than for the low energy neutrons.

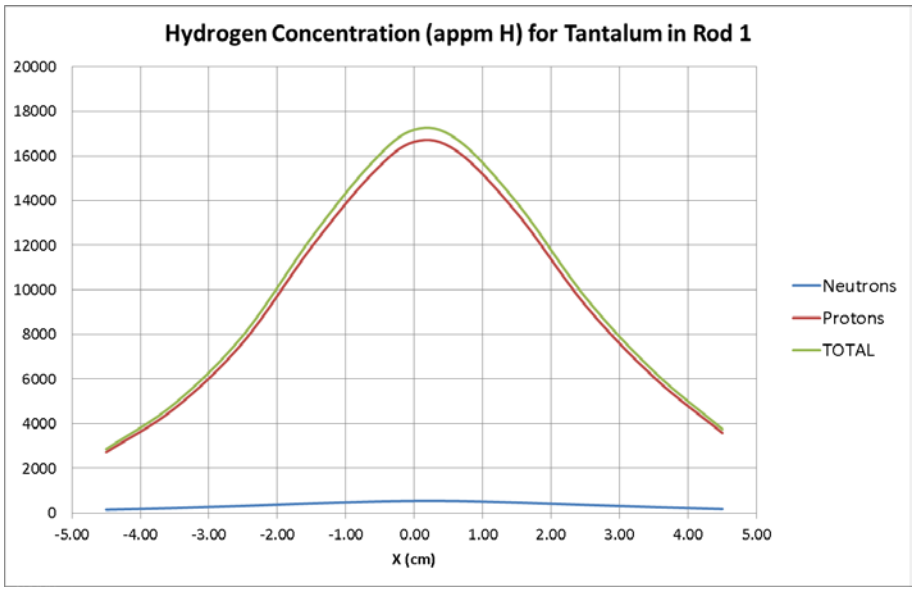

Figure 4.26 Hydrogen concentration for Tantalum in Rod 1

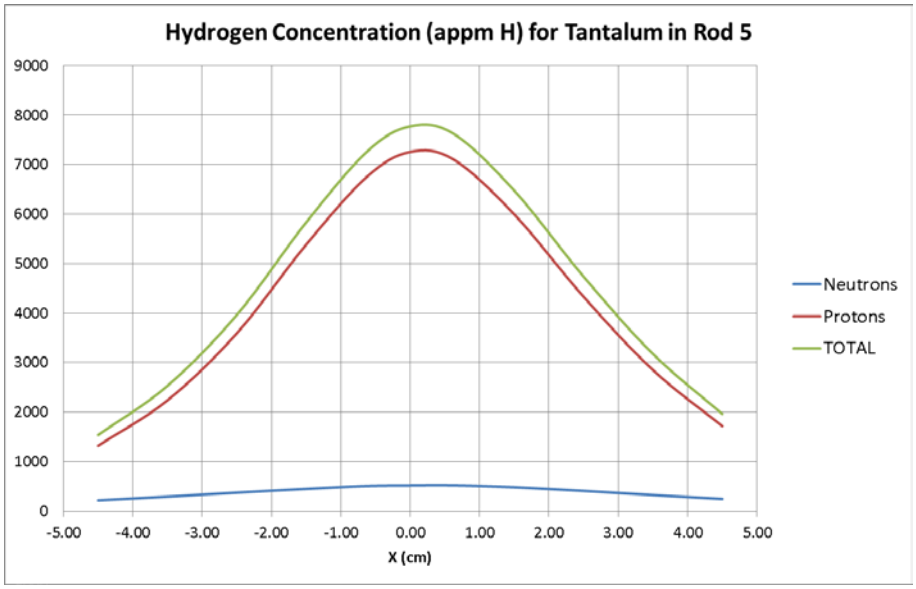

Figure 4.27 Hydrogen concentration for Tantalum in Rod 5

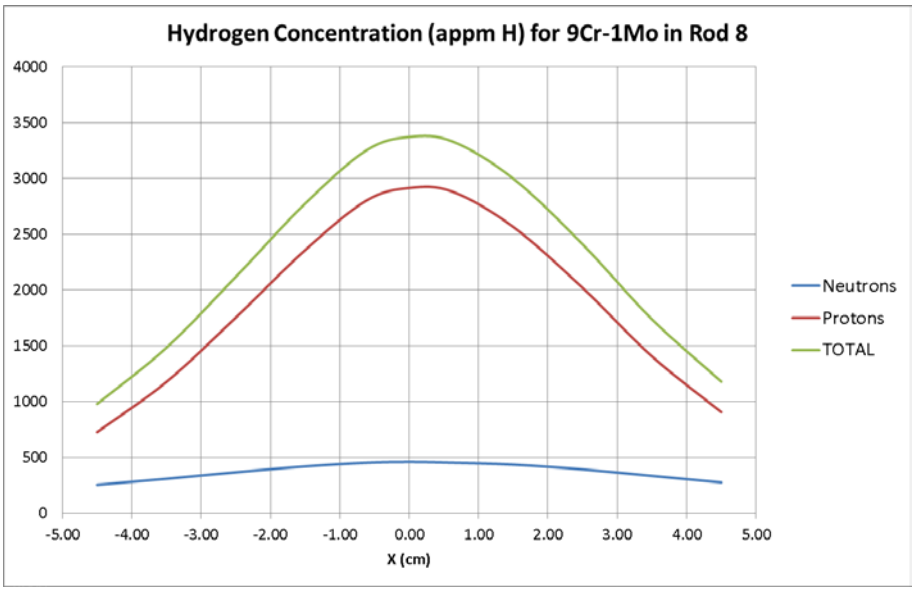

Figure 4.28 Hydrogen concentration for 9Cr-1Mo in Rod 8

5. CONCLUSIONS

The irradiation parameters of displacement per atom plus Hydrogen and Helium concentration have been calculated based on a MCNPX simulation for assessing the radiation damage of STIP VI – Target 9. The simulation model has been updated accordingly with STIP VI – Target 9 materials and geometry data. The source definition on the MCNPX input file is implemented from the gamma mapping performed at the irradiated Target 9. The simulation is providing the proton and neutron fluence over all points of interest. It allows the calculation of the irradiation parameters afterwards by multiplying the fluence with the corresponding material cross section data.

The maximum proton fluence is 8.33×10^{25} p/m^2 and it is obtained at the center of Tube T, which is located in Row 0. Then, the proton fluence is decreasing along the target due to scattering interactions. The maximum proton fluence reached in the similar experiment performed with STIP IV – Target 6 was 6.5×10^{25} p/m^2 which stands for an increase close to 30%.

The neutron flux starts to increase from Row 0 till Row 8 where the maximum value is reached, being 4.19×10^{14} n/(cm^2·s·mA). After that, the neutron flux is decreasing progressively along further rods because the proton flux is also decreasing due to their loss of energy in scattering interactions which results in less spallation reactions. The maximum neutron flux reached in the similar experiment performed with STIP IV – Target 6 was 2.30×10^{14} n/(cm^2·s·mA) which stands for an increase of more than 80%.

The maximum Energy Deposition is obtained in the cladding of Rod 1, which is located in Row 2, with a value of 400.32 W/(cm^3·mA). The energy deposition is also decreasing from Row 2 to Row 36 with the exception of Row 16, where Rod 6 is placed. The cladding of this rod is made of steel which produces the expected increase in the energy deposition.

The irradiation parameters calculated at the center of the calotte are providing the following maximum values: 8.85 dpa, 2447.36 appm He and 4853.74 appm H. Regarding the SHT, the maximum values are obtained at the middle part (Row 16) of the target resulting in an irradiation damage of 3.14 dpa, 17.63 appm He and 71.64 appm H.

The maximum displacement per atom is obtained for Zircaloy-2 in Rod 1, placed in Row 2, with a value of 72.07 dpa. Regarding the Helium and Hydrogen production, the maximum values are obtained for Tantalum in Rod A, placed in Row 1, with a value of 3628.94 appm He and 17418.39 appm H. The different materials in the specimen rods of STIP IV – Target 6 were irradiated up to 27 dpa and 2300 appm He. An exhaustive analysis of the radiation damage results obtained in the present project is being done at PSI by experts in material science. However, a first overview of the results is briefly commented in the following lines.

The Helium to displacement per atom ratio is widely used for assessing and comparing the radiation damage in different irradiation environments. High energy protons are inducing a high production rate of Helium and Hydrogen in materials. For most of the material involved in each scenario, this ratio value is around 10-15 appm He/dpa in fusion reactors and lower than 1 appm He/dpa in fission reactors. In spallation targets, this value is expected to be up to 100 appm He/dpa. *Figure 5.1* is showing the maximum values of this ratio in Rod 1 for each material. The maximum value of Helium to dpa ratio has been obtained in Rod 1 for Silicon Carbide becoming 181.51 appm He/dpa. Although this value seems a bit higher than expected, the SiC material is showing the same behavior in fusion reactor which its reference value is also increased up to 100 appm He/dpa or even more. Actually, the fusion community is doing a lot of research on this material nowadays because it could have an important role in the future.

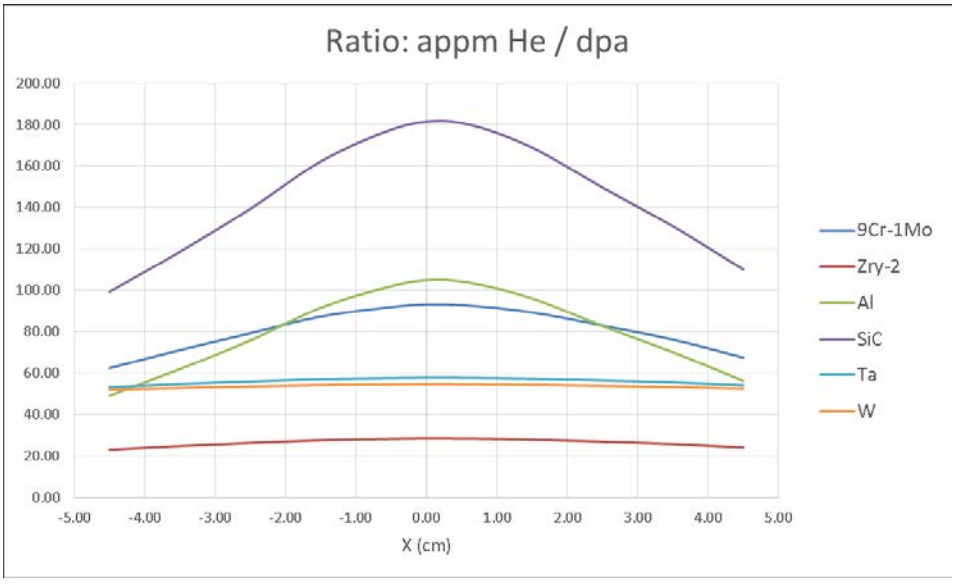

Figure 5.1 appm He/dpa ratio in Rod 1

TEMPORARY PLANNING AND COSTS

The planning followed during the project is presented in *Figure T1*. The project started with a familiarization in MCNPX to perform the model adjustments according to STIP VI – Target 9, afterwards. Later on, some simulations were run at the same time that the model was being developed to improve and verify it. Finally, the simulation results were analyzed and the final report and presentation were done to conclude the project. The time required in September for finishing up all the documentation required by the university has been added without considering any cost in the project.

April	May		June		July		August		September	
16-30	1-15	16-31	1-15	16-30	1-15	16-31	1-15	16-31	1-15	16-30
Familiarization with MCNPX										
		MCNPX simulation model adjustments								
			MCNPX simulations							
				Analysis of the results						
							Final report and presentation			

Figure T1 Temporary planning of the project

The total cost of the project has been divided in the following budget lines: Office equipment & Material, Overhead Cost and Staff Cost. The project has been done entirely in Switzerland during four and a half months. So, trips and other administrative documents that could be concerned are not taken into account. Taxes are not considered and the staff cost has been estimated as net salary. The total cost of the project with all budget lines considered is presented in the following table:

PROJECT COST	CHF
Office Equipment and Material	**1,300.00**
License MCNPX	800.00
License Microsoft Office	150.00
Equipment amortization	300.00
Others (sheets, pens, folders)	50.00
Overhead Cost	**150.00**
Electricity and water	150.00
Staff Cost	**11,250.00**
Internship (Junior)	9,000.00
Supervisor (Senior)	2,250.00
TOTAL	**12,700.00**

Table C1 Total cost of the project

ENVIRONMENTAL IMPACT

The project has been done in the framework of the SINQ Target Irradiation Program (STIP) which is involving many powerful research centers worldwide. STIP experiments are aimed to analyze the radiation damage induced by spallation reactions in different structural materials which is really interesting for the nuclear fusion community. It is also providing relevant data for developing future spallation sources as well as advanced spallation targets.

The environment is not receiving any significant direct impact due to the project developed. The fact is that the project is based on a Monte Carlo simulation which avoids all the environmental impact concerned during the construction, maintenance and dismantling of such facilities necessary to perform these kind of experiments.

ACKNOWLEDGEMENTS

I would like to express my deepest gratitude to my supervisor, Dr. Yong Dai, who provided me the opportunity of working in such powerful research center as PSI and also assisted me during the entire project being really kind and always available for all doubts I had.

I would also like to acknowledge the generous assistance provided by Dr. Ryan Bergmann and Dr. Michael Wohlmuther during my entire work on the MCNPX simulation. I am really grateful to say that I have learned a lot about MCNPX and that would not have been possible without them.

Finally, I would like to thank all people who have been close to me during my internship because I spent a really good time with them and it also allows me to go every day to work full of energy. So, thank you very much to my colleagues at work and the Guesthouse people. It has been a wonderful experience to work and live with you.

REFERENCES

[1] W. Wagner. TARGET OPERATION AT THE HIGH-POWER NEUTRON SPALLATION SOURCE SINQ – SAFETY AND RELIABILITY ISSUES. Paul Scherrer Institut, Villigen PSI, Switzerland.

[2] Website of the International Atomic Energy Agency (IAEA) providing Nuclear Data Services. www-nds.iaea.org/spallations

[3] Y. Dai, G.S. Bauer. Status of the first SINQ irradiation experiment, STIP-I. Journal of Nuclear Materials 296 (2001) 43-53.

[4] Y. Dai, X. Jia, R. Thermer, D. Hamaguchi, K. Geissmann, E. Lehmann, H.P. Linder, M. James, F. Gröschel, W.Wagner, G.S. Bauer. The second SINQ target irradiation program, STIP-II. Journal of Nuclear Materials 343 (2005) 33-44.

[5] MCNP — A General Monte Carlo N-Particle Transport Code, Version 5. Volume I: Overview and Theory. X-5 Monte Carlo Team. April 24, 2003 (revised 10/03/05).

[6] J. Kenneth Shultis and Richard E. Faw. AN MCNP PRIMER. AN INTRODUCTION TO THE MCNP CODE. Dept. of Mechanical and Nuclear Engineering. Kansas State University.

[7] Paul Scherrer Institut (PSI) Website: www.psi.ch

[8] W. Lu and M. S. Wechsler, Y. Dai. PRELIMINARY REPORT: CALCULATIONS OF RADIATION DAMAGE TO SINQ TARGET 5 (STIP III).

[9] Y. Dai, R. Brun, W. Gao, K. Geissmann, S. Hahl, H. Hou, Y. Huang, H.P. Linder, B. Long, A. Spahr , P. Vontobel , W. Wagner , H.L. Wang, L. Zanini. The fourth SINQ Target Irradiation Program, STIP-IV. Journal of Nuclear Materials 431 (2012) 2-9.

[10] Personal communication, Mr. Yong Dai (Confidential).